

# Sediment controls on the transition from debris flow to fluvial channels in steep mountain ranges

Alexander B. Neely<sup>1</sup> | Roman A. DiBiase<sup>1,2</sup>

<sup>1</sup>Department of Geosciences, Pennsylvania State University, University Park, Pennsylvania, USA

<sup>2</sup>Earth and Environmental Systems Institute, Pennsylvania State University, University Park, Pennsylvania, USA

## Correspondence

Alexander B. Neely, University of Tübingen, 72076, Tübingen, Germany.

Email: [abngeo@ gmail.com](mailto:abngeo@ gmail.com)

## Funding information

National Science Foundation, Grant/Award Number: EAR-1608014

## Abstract

Steep channel networks commonly show a transition from constant-gradient colluvial channels associated with debris flow activity to concave-up fluvial channels downstream. The trade-off between debris flow and fluvial erosion in steep channels remains unclear, which obscures connections among topography, tectonics, and climate in steep landscapes. Here, we analyze steep debris-flow-prone channels across the western United States and observe: (1) similar maximum channel gradients across a range of catchment erosion rates and geologic settings; and (2) lengthening colluvial channels with coarsening sediment cover. Following this compilation, we hypothesize that steep channel gradients are controlled by two competing thresholds of motion for bed-sediment cover: bed failure by mass-wasting and fluvial entrainment. We use downstream patterns in discharge, channel geometry, and sediment size to calculate discharges needed to mobilize sediment cover by both mechanisms across channels in the San Gabriel Mountains (SGM) and northern San Jacinto Mountains (NSJM) in southern California. Across steep colluvial channels in both landscapes, decadal discharges are below fluvial entrainment thresholds but above mass-wasting entrainment thresholds for  $D_{50}$  (median) sediment sizes, consistent with recent debris flows captured by repeat imagery. Colluvial channel gradient is similar despite  $> 3\times$  contrasts in surface sediment grain size. In concave-up fluvial channels downstream, decadal discharges exceed fluvial entrainment thresholds, and mass-wasting is not predicted on lower gradients. In both landscapes, fluvial channels steepen downstream compared to gradients needed to mobilize sediment cover, which we interpret to reflect downstream increases in sediment flux. Coarser sediment supply in the NSJM than the SGM increases fluvial entrainment thresholds, which increases total channel relief in the NSJM by (1) lengthening colluvial channels shaped by debris flows and (2) increasing fluvial channel gradients. Our compilation and downstream analysis show how differing sensitivity of fluvial and debris flow processes to sediment grain size impacts the relative relief of colluvial and fluvial regimes in headwater channel networks.

## KEY WORDS

channel, debris flow, fluvial, grain size, sediment, steep

## 1 | INTRODUCTION

Headwater channel networks with gradients steeper than  $\sim 10\%$  contribute significantly to mountain range relief (DiBiase et al., 2018; Stock & Dietrich, 2003), serve an important role in the storage and

delivery of sediment between hillslopes and downstream rivers (Benda, 1990; Benda et al., 2005), and are a source for destructive debris flows. However, the sediment transport and incision processes that shape headwater channel networks are poorly understood compared to lower-gradient ( $< 10\%$ ) river systems, where a robust

conceptual framework links channel gradient, sediment transport, and incision (e.g., Lague, 2014; Sklar & Dietrich, 2004; Whipple et al., 2022). Sediment transport is more intermittent in headwater channels, which makes field observation difficult, and constraints on initial motion thresholds are sparse. Coarse sediments supplied from landslides, debris flows, and rockfalls complicate flow dynamics in smaller, steeper channels characteristic of headwater networks, weakening assumptions built into models for larger rivers (Ferguson, 2007; Palucis & Lamb, 2017). Additionally, headwater channel networks are often traversed by debris flows, and mechanistic models describing debris-flow incision are poorly constrained due to difficulties in the field measurement of key model parameters (McGuire et al., 2022; Stock & Dietrich, 2006).

Topographic analysis of steep headwater channel networks show that their longitudinal profiles differ from typical concave-up scaling observed in lower-gradient rivers. In the uppermost portions of headwater channel networks, there is often limited or no change in channel slope with distance downstream in what are termed “colluvial”

channels, in contrast to “fluvial” channels where slope decreases systematically with distance downstream (i.e., concave-up profile) (Figure 1; Montgomery & Foufoula-Georgiou, 1993). The upstream extent of the concave-up longitudinal profile is commonly interpreted as a morphologic signature of fluvial channel heads (Clubb et al., 2014; Montgomery & Dietrich, 1988), and steep, constant-slope colluvial channels upstream from this position are often associated with debris-flow activity (Stock & Dietrich, 2003).

Yet, numerous studies document debris flows that initiate on steep slopes but deposit in downstream fluvial systems with channel gradients as low as 5–10% (Benda, 1990; Berti et al., 1999; Daido, 1971; Hürlimann et al., 2003; Hungr et al., 2005). Certain debris flows show decimeters to meters of scour (Berti et al., 1999; Hungr et al., 2005), including into rock (Hsu, 2015), and debris flows frequently impact catchment outlets on urbanized fans with drainage areas of 10–100 km<sup>2</sup> (Gartner et al., 2014). For these reasons, debris flows have been considered effective geomorphic agents at channel gradients as low as 3% and drainage areas of > 10 km<sup>2</sup> (Stock &

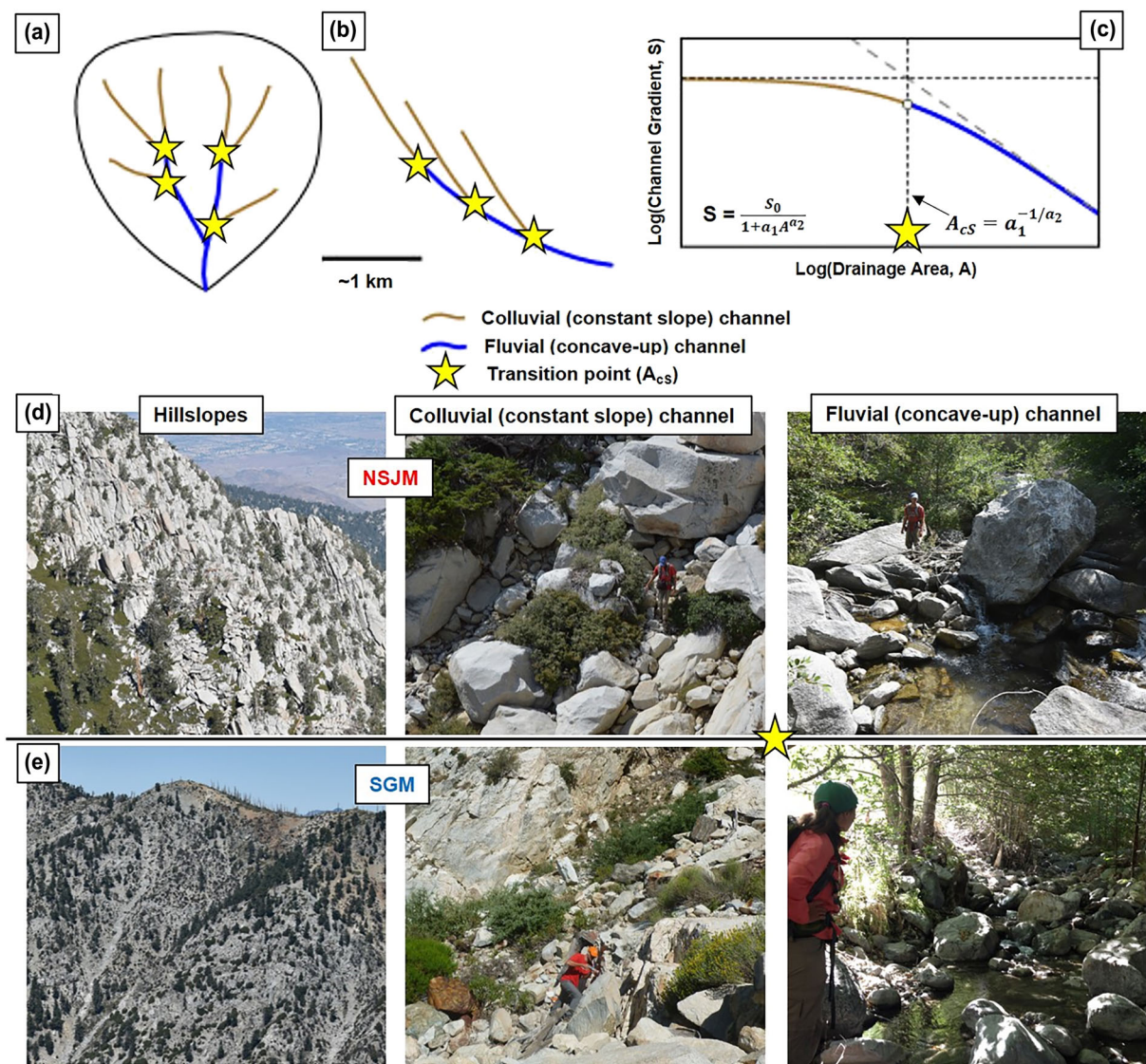


**FIGURE 1** (A–C) Definition sketches showing steep headwater channel networks composed of colluvial and fluvial channels in: (A) map view; (B) longitudinal-profile view; (C) slope–area space. Stars indicate transition from colluvial to fluvial channels (commonly occurring at tributary junctions). Field photographs from the northern San Jacinto Mountains (NSJM, D) and San Gabriel Mountains (SGM, E) show transition from hillslopes (left column) downstream through colluvial channels and fluvial channels (center and right columns respectively) [Color figure can be viewed at [wileyonlinelibrary.com](http://wileyonlinelibrary.com)]

Dietrich, 2006), but the mechanistic connection between debris-flow activity and landscape evolution over these reaches is less understood.

The response of colluvial channel morphology to tectonics, climate, or rock strength is varied, but few field studies have been conducted to inform process-based erosion models (McGuire et al., 2022). Colluvial channel gradient was found to increase with increasing rock uplift and erosion rate in the Siwaliks Hills of central Nepal (Lague & Davy, 2003). However, the gradient of colluvial channels showed less variation in the steeper landscapes of the Oregon Coast Range (OCR) and San Gabriel Mountains (SGM); instead, the length of colluvial channels was found to increase with increasing erosion and rock uplift rates in these sites (DiBiase et al., 2012; Penserini et al., 2017). Between two steep landscapes with contrasting bedrock fracture densities in the eastern SGM and the northern San Jacinto Mountains (NSJM) in California, the gradient of colluvial channels also did not vary, but the extent, and thus relief of colluvial channel networks was greater in the NSJM, which are underlain by less-fractured bedrock (DiBiase et al., 2018). In each of these studies, a lack of data constraining channel cross-sectional geometry, bed sediment cover, and runoff make it challenging to directly compare channel morphodynamics across different landscapes.

Knowledge gaps persist when assessing sediment transport and bedrock incision in steep headwater channel networks, which include both colluvial and fluvial channels. For example, how do changes in bed sediment size and therefore fluvial entrainment thresholds affect the morphodynamics of steep channels (e.g., Lamb et al., 2008; Prancevic et al., 2014)? Is bed sediment mobilized primarily by mass-wasting in steep channels, and if so, how far downstream do these flows travel and sculpt channels (Stock & Dietrich, 2006)? Do these factors correspond with consistent changes in longitudinal profile geometry that are seen in many landscapes between colluvial channels and fluvial channels downstream (e.g., Stock & Dietrich, 2003)?

We address these knowledge gaps using two approaches that leverage field surveys and an increasing availability of high-resolution imagery and topography data. First, we present a compilation of headwater channel longitudinal profiles where high-resolution topography, catchment averaged erosion rates, and field measurements of bed sediment grain size are co-located. Second, we analyze the morphology of headwater channels that span both colluvial and steep fluvial channels in the SGM and NSJM in southern California, where field data constrain downstream patterns in sediment grain size, channel width, and discharge. We use the dense array of field measurements in the SGM and NSJM to model patterns of sediment mobility by fluvial and debris flow processes in these landscapes, and we compare our model predictions with observations of sediment motion recorded by repeat aerial imagery that brackets recent storms.

## 2 | COMPILATION OF HEADWATER CHANNEL MORPHOLOGIES IN STEEP LANDSCAPES OF THE WESTERN UNITED STATES

We compiled existing and new data from steep landscapes in the western United States to examine the range of headwater channel morphologies in the context of available catchment-averaged erosion

rates and co-located bed sediment grain size surveys. We focused on sites with airborne-lidar-derived topographic data, catchment erosion rates from cosmogenic nuclides, and grain size data measured near the transition from colluvial channels to concave-up fluvial channels (DiBiase & Ferrier, 2020; Dietrich, 2014; DOGAMI, 2011; Moon, 2012; Neely, 2019; US Geological Survey, 2020) (Figure 2).

Our compilation includes localities across various tectonic, lithologic, and climatic settings: the southern California transverse ranges of the SGM, NSJM, and San Bernardino Mountains (SBM) (Binnie et al., 2007; DiBiase et al., 2010; Heimsath et al., 2012; Neely et al., 2019); the northern California Coast Ranges (NCCR) including the King Range and South Fork Eel River (Fuller et al., 2009; Moon et al., 2018); the OCR (Penserini et al., 2017); and the Guadalupe Mountains (GM) of New Mexico/Texas (Tranel & Happel, 2020). Each of these localities contains published erosion rates derived from cosmogenic radionuclides that integrate over  $10^2$ – $10^5$  year timescales. We supplement existing surface sediment grain size data with new field measurements from the King Range in the NCCR, SBM, and GM that align with published erosion rate sample locations (see Table S1 and Supporting Data S1). Bedrock lithology ranges from crystalline basement rocks (SGM, NSJM, SBM) to clastic (NCCR and OCR) and carbonate (GM) sedimentary rocks. The southern California (SGM, NSJM, SBM) and GM sites are broadly characterized by seasonal semi-arid climates with chaparral vegetation cover at low elevations (1–2 km) transitioning to forest cover at higher elevations (SGM, NSJM, SBM, and GM), whereas the NCCR and OCR sites are characterized by wetter coastal-Mediterranean and temperate climates with continuous forest cover (Figure 2).

### 2.1 | Topographic analysis of headwater channel networks

Stock & Dietrich (2003) proposed an empirical relationship between local channel gradient,  $S$ , and upstream contributing area,  $A$ , to describe the transition from constant-gradient colluvial channels to concave-up fluvial channels in headwater networks:

$$S = \tan \theta = \frac{S_0}{1 + a_1(A^{a_2})}, \quad (1)$$

where  $\theta$  is the channel slope angle,  $S_0$  is a threshold gradient asymptotically approached at low drainage area, and  $a_1$  and  $a_2$  are coefficients that describe the transition to fluvial channels at larger drainage area. At large drainage areas, Equation (1) asymptotes to the commonly used power-law relationship of Flint's law for fluvial channels (Flint, 1974), with the coefficient  $a_2$  corresponding to the fluvial concavity index (Whipple et al., 2022). We define the transition from colluvial to fluvial channels by a critical drainage area,  $A_{cs}$ , that reflects the drainage area at which the fluvial (power-law) slope-area scaling is projected to intersect the threshold gradient,  $S_0$  (Figure 1; McGuire et al., 2022):

$$A_{cs} = a_1^{-\frac{1}{a_2}}. \quad (2)$$

Mechanistic explanations for Equation (1) commonly consider a different scaling between channel slope and bedrock erosion for

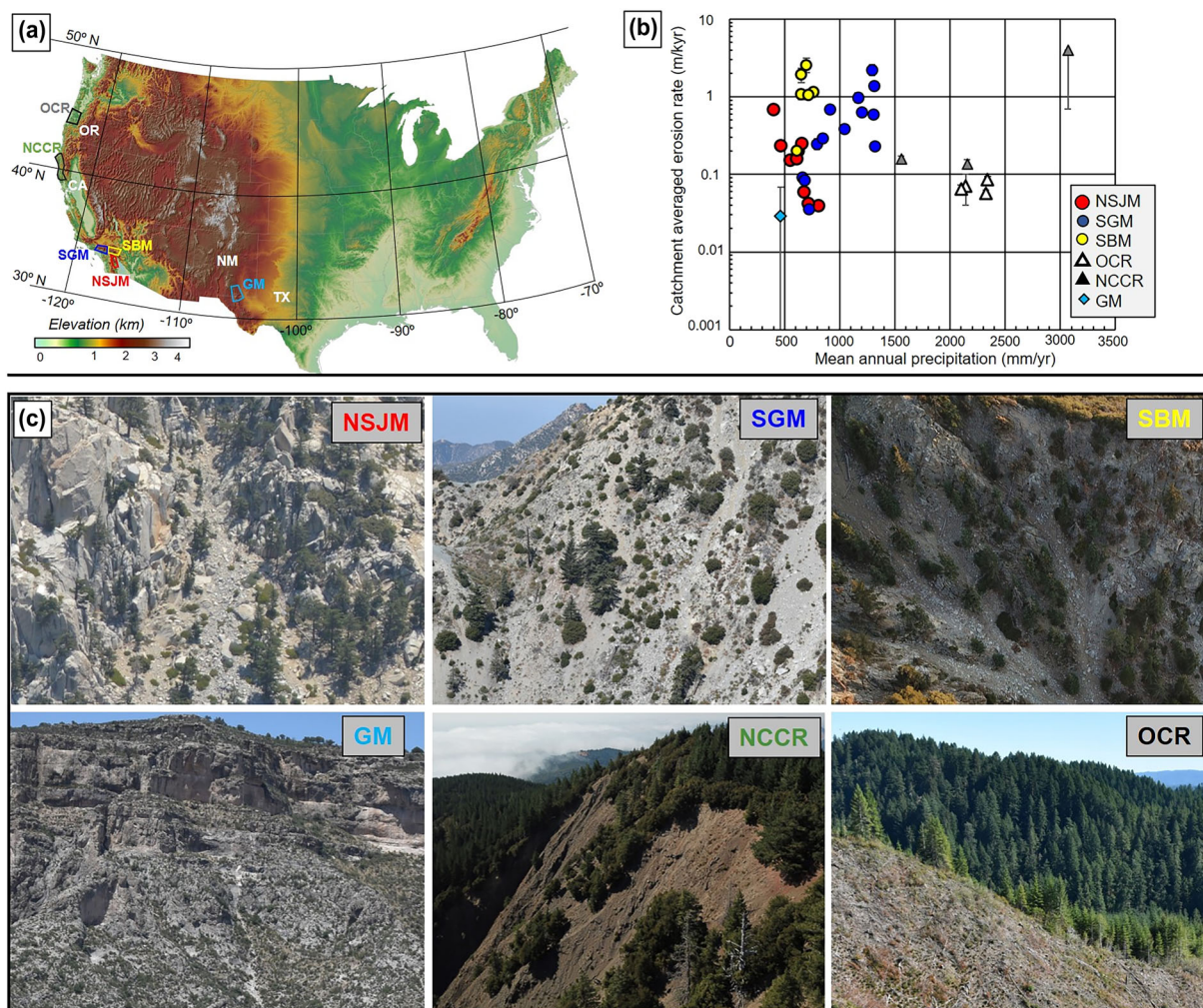


**FIGURE 2** (A) Location of western United States headwater channel compilation and surrounding topography. (B) Range in catchment averaged erosion rates and mean annual precipitation range across compiled basins underlain with crystalline bedrock (circles), clastic sedimentary bedrock (triangles), and carbonate sedimentary rock (diamond). Mean annual precipitation normals are determined for each catchment from 1991 to 2020 (PRISM Climate Group, Oregon State University, <https://prism.oregonstate.edu>, data created November 2021, accessed 14 December 2022). (C) Field photographs of headwater channel and hillslope regions (NSJM: northern San Jacinto Mountains; SGM: San Gabriel Mountains; SBM: San Bernardino Mountains; GM: Guadalupe Mountains; NCCR: northern California Coast Ranges; OCR: Oregon Coast Range) [Color figure can be viewed at [wileyonlinelibrary.com](http://wileyonlinelibrary.com)]

debris flow and fluvial incision processes (McGuire et al., 2022). The empirical equation provides a useful framework for quantifying the relative length and relief of colluvial channels in the context of variable tectonic, climatic, or geologic settings (Stock & Dietrich, 2003).

For each of the landscapes analyzed, we extracted downstream changes in channel gradient along steepest-descent flow paths from airborne lidar topography resampled to 5 m resolution using TopoToolbox (Schwanghart & Scherler, 2014). Channel gradients from all tributaries ( $A > 10^3 \text{ m}^2$ ) within a watershed were discretized into 100 logarithmically spaced bins of drainage area, and the mean gradient of each drainage area bin was recorded at the median drainage area position of the bin. We use a cutoff drainage area of  $10^3 \text{ m}^2$  to define the upper limit of colluvial channels based on prior analyses in the OCR and SGM (DiBiase et al., 2012; Penserini et al., 2017). For each landscape, we fit  $S_0$ ,  $a_1$ , and  $a_2$  to the log-transformed, binned channel slope-area data using an iterative summed-least squares regression (e.g., Penserini et al., 2017).

## 2.2 | Compilation of erosion rate and grain size data

For consistency, erosion rates derived from beryllium-10 ( $^{10}\text{Be}$ ) concentrations of detrital sediment were recalculated from  $^{10}\text{Be}$  concentrations, sampled watershed elevations, and laboratory standards reported in publications using the CRONUS-Earth online calculator (<http://hess.ess.washington.edu>, version 3; Balco et al., 2008) (see Table S1). For the GM site, which did not have detrital erosion rate estimates, we used published chlorine-36 ( $^{36}\text{Cl}$ ) derived bedrock erosion rates (Tranel & Happel, 2020). Because we focus on small ( $< 20 \text{ km}^2$ ) watersheds with broadly uniform topographic characteristics and minimal landslide influence or sediment storage, we assume that cosmogenic radionuclide concentrations reflect steady-state erosion rates throughout each watershed.

Grain size data come from a mix of published and new surveys. For the Elder Creek (NCCR) and OCR sites, we used existing bed sediment grain size surveys (Fratkin et al., 2020; Scheingross et al., 2013).

Grain size data from the SGM and NSJM (Neely & DiBiase, 2020) are described in more detail in Section 4.2.4. Grain size data from the Guadalupe Mountains (GM) (Loucks, 2020), King Range (NCCR), and SBM were measured directly during field campaigns between 2017 and 2019 using a combination of pebble counts and grid-by-number surveys performed on scaled ground-based and aerial imagery (see Table S1; Supporting Data S1, Neely et al., 2021).

## 2.3 | Observed variations in headwater channel morphologies

The compilation of headwater channel profiles in Figure 3 reveals large differences in headwater channel morphology among the landscapes compared. The total relief of the upstream (colluvial) portion of the headwater channel network can vary by a factor of 10 between endmembers in the OCR and NSJM, despite similar catchment averaged erosion rates (Figure 3E). Although catchments with the slowest erosion rates generally have the lowest colluvial channel gradient,  $S_0$  remains similar across a wide range of erosion rates in steep landscapes. Maximum colluvial slopes in sediment-mantled channels appear to reflect the frictional stability of loose sediment ( $S_0 = 0.7 - 0.8$ ). Steeper maximum colluvial channel slopes,  $S_0 > 0.8$ ,

are observed where bedrock cliffs comprise a large fraction of headwater catchments in the NSJM and SGM (Neely et al., 2019), and extensive cliff exposure results in a fraction of the colluvial network comprising of bare-bedrock chutes (see Figure S1 in Supporting Information). Overall,  $S_0$  increases with increasing sediment grain size but does not explain the wide range of colluvial channel relief observed (30–1400 m) (see Figure S2). Much of the variation in colluvial channel relief is instead accommodated by differences in the length of colluvial channels, as expressed by  $A_{CS}$  (Figure 3).

Among the landscapes analyzed,  $A_{CS}$  ranges from  $\sim 10^4$  to  $10^6 \text{ m}^2$  and shows a different sensitivity to changes in catchment erosion rate and sediment grain size. Although colluvial channels tend to be less extensive (lower  $A_{CS}$ ) in lower-sloping, slower-eroding landscapes, for steeper landscapes there is no clear relationship between  $A_{CS}$  and erosion rate (Figure 3C). Rather, colluvial channel length appears more sensitive to changes in bed sediment grain size among the compiled landscapes (Figure 3D). Consequently, the relative relief of colluvial channels shows a different dependence to changes in bed sediment grain size and sediment flux delivered from hillslopes, particularly across steep watersheds with contrasting sediment grain size inputs from hillslopes (Sklar et al., 2017).

Isolating sediment size controls on  $S_0$  and  $A_{CS}$  across each of these landscapes is limited by the lack of data constraining hydrology,

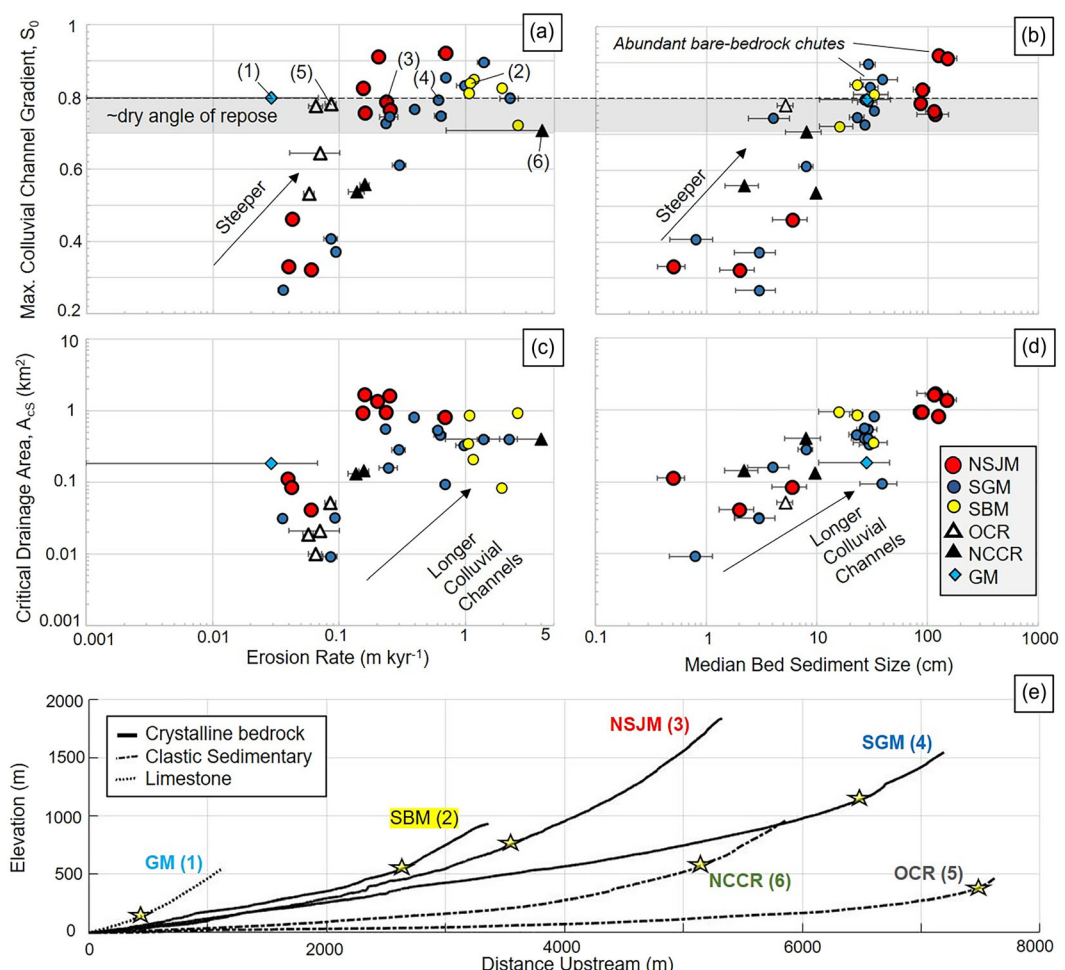


**FIGURE 3** Variation in maximum colluvial channel slope,  $S_0$  (A, B) and colluvial channel length expressed through  $A_{CS}$  (C, D, Equation 2) across compiled headwater channel networks in the western United States (locations and abbreviations as in Figure 2). (E) Example longitudinal profiles of headwater channels from each landscape indicating transition point from constant gradient colluvial channel to concave-up fluvial channels (yellow stars). Numbered profiles (E) correspond to labeled data points in (A) [Color figure can be viewed at [wileyonlinelibrary.com](https://onlinelibrary.wiley.com)]

channel geometry, and bedrock erodibility, which also affect the coupling between channel morphology, sediment grain size, and sediment transport (e.g., Sklar & Dietrich, 2004; Whipple et al., 2022). Thus, for the rest of this article, we focus on two landscapes, the SGM and NSJM, where downstream trends in each of these variables can be quantified using high resolution topography and imagery data, field surveys, and streamflow records. Data coverage across steep channel networks in the SGM and NSJM enables comprehensive comparison between channel morphology and bed sediment mobility. Particularly, measurements span the transition from constant-gradient colluvial channels to concave-up fluvial channels in two landscapes (SGM, NSJM) that have broadly contrasting sediment grain size inputs.

### 3 | THRESHOLD HYPOTHESIS FOR HEADWATER CHANNEL NETWORKS

At steady state (erosion rate equal to rock uplift rate), headwater channels serve the dual role of transporting sediment delivered from upstream and eroding underlying bedrock at rock uplift rates. Channel gradient,  $S$ , can be interpreted to represent the sum of three factors (Finnegan et al., 2017; Lai et al., 2021; Sklar & Dietrich, 2006):

$$S = S_D + S_{Qs} + S_E, \quad (3)$$

where  $S_D$  is the slope required for the initial motion of sediment cover,  $S_{Qs}$  is the slope needed to transport the flux of sediment delivered from upstream, and  $S_E$  is the slope needed for the channel to incise bedrock at the rate of rock uplift.

Here, we investigate the hypothesis that the morphology of headwater channels is most sensitive to a grain-size-dependent initial motion threshold ( $S \approx S_D$ ) in both steep, constant-gradient colluvial channels and concave-up fluvial channels (Phillips & Jerolmack, 2016). We start with this hypothesis as the simplest explanation for the lengthening of colluvial channels with increasing grain size observed in Figure 3(D). We describe two frameworks for calculating sediment initial motion thresholds, using fluvial traction (Section 3.1) or in-channel mass wasting (Section 3.2) as the sediment mobilization process.

#### 3.1 | Incipient motion of sediment in fluvial environments

The initial motion by fluvial traction of streambed sediment with a median grain diameter  $D_{50}$  can be described using a Shields criterion to determine the critical shear stress for initial motion,  $\tau_{cf}$ :

$$\tau_{cf} = \tau_{cf}^* (\rho_s - \rho_w) g D_{50}, \quad (4)$$

where  $\tau_{cf}^*$  is the non-dimensional critical fluvial Shields stress,  $\rho_s$  and  $\rho_w$  are the densities of sediment and water, and  $g$  is gravitational acceleration.

Although typically constrained to a narrow interval between 0.03 and 0.06 for low-gradient gravel-bedded rivers,  $\tau_{cf}^*$  tends to be higher in steeper channels due to changes in bed sediment stability and increases in relative roughness for shallow flows (Lamb et al., 2008;

Prancevic & Lamb, 2015a; Zimmermann et al., 2010). Because downstream changes in channel slope may decouple from downstream coarsening and fining trends in headwater channels (e.g., Brummer & Montgomery, 2003; Fratkin et al., 2020; Neely & DiBiase, 2020), we use an approach where  $\tau_{cf}^*$  varies directly with relative roughness, rather than using channel slope as a proxy (e.g., Lamb et al., 2008). We use an empirically derived relationship between flow resistance and  $\tau_{cf}^*$ , which accounts for decreases in flow velocity with increasing bed roughness in the context of critical discharges needed to mobilize bed sediment (Parker et al., 2011; Prancevic & Lamb, 2015b):

$$\tau_{cf}^* = C_1 \left( \frac{1}{F^2} \right)^{C_2}, \quad (5)$$

where  $F$  is the Darcy–Weisbach friction factor and  $C_1$  and  $C_2$  are empirical constants (Prancevic & Lamb, 2015b).

The relationship between the friction factor,  $F$ , and fluvial critical Shields stress,  $\tau_{cf}^*$ , paired with a prescribed channel geometry, allows the calculation of a critical flow depth,  $h_c$ , needed to mobilize sediment at any point in the channel network. We assume a trapezoidal channel cross-section to relate channel cross-sectional area,  $A_{xs}$ , to centerline flow depth,  $h$ .

$$A_{xs} = w_b h + \frac{h^2}{\tan \alpha}, \quad (6)$$

where  $w_b$  is the basal width and  $\alpha$  is the bank angle. The hydraulic radius,  $R_h$ , is:

$$R_h = A_{xs}/p, \quad (7)$$

where  $p$  is the wetted perimeter of the channel defined for a trapezoidal channel as:

$$p = w_b + 2\sqrt{h^2 + (h/\tan \alpha)^2}. \quad (8)$$

The friction factor,  $F$ , is determined using an empirical relationship between  $F$  and the relative roughness defined by the  $D_{84}$  sediment size following Ferguson (2007):

$$F = \frac{U}{\sqrt{g R_h \sin \theta}} = \frac{Fa_1 Fa_2 \left( \frac{R_h}{D_{84}} \right)}{\left( Fa_1^2 + Fa_2^2 \left( \frac{R_h}{D_{84}} \right)^{5/3} \right)^{1/2}}, \quad (9)$$

where  $U$  is cross-sectional averaged flow velocity,  $\theta$  is the channel slope angle over the reach length analyzed, and  $Fa_1$  and  $Fa_2$  are empirically derived constants. Finally, we define water discharge,  $Q$ , and bed shear stress,  $\tau$ , assuming steady, uniform flow conditions:

$$Q = U A_{xs}, \quad (10)$$

$$\tau = \rho_w g R_h \sin \theta. \quad (11)$$

The critical discharge,  $Q_{cf}$ , and critical flow depth for initial sediment motion by fluvial transport,  $h_{cf}$ , can then be calculated numerically by

solving Equations (4)–(11) provided there are estimates of channel slope,  $\theta$ , channel width,  $w_b$ , bank angle,  $\alpha$ , and the  $D_{50}$  and  $D_{84}$  of bed material grain size.

### 3.2 | Incipient motion by mass wasting failure of the channel bed

A second threshold-of-motion criterion for bed sediment relates to the failure of channel bed material along a discrete failure plane in a shallow landslide. This threshold-of-motion criterion can be described by an infinite-slope, Mohr-Coulomb slope-stability model that depends on the internal angle of friction, density, and porosity of channel bed sediment (Takahashi, 1978). Bed failure typically occurs when flows are high enough to saturate channel bed sediment and generate surface runoff (Prancevic et al., 2014). An analogous Shields criterion can be described by a critical shear stress needed to initiate discrete failure of channel bed sediments (Prancevic et al., 2014):

$$\tau_{cm}^* = (1 - \eta)(\tan \varphi - \tan \theta) - \frac{\rho_w}{\rho_s - \rho_w} \tan \theta \quad (12)$$

$$\tau_{cm} = \tau_{cm}^* (\rho_s - \rho_w) g D_{50}, \quad (13)$$

where  $\eta$  is bed porosity and  $\varphi$  is the internal angle of friction of the bed sediment cover. Although  $\eta$  and  $\varphi$  are difficult to constrain in coarse-grained colluvial channels at the scale of field studies, Prancevic et al. (2014) showed that bed failure by mass wasting ( $\tau_{cm}^* < \tau_{cf}^*$ ) is favored on steep ( $> 23^\circ$ ) channel slopes that approach frictional stability limits and individual entertainment of grains ( $\tau_{cm}^* > \tau_{cf}^*$ ) is favored on channel slopes less than  $\sim 23^\circ$  ( $\tan \theta < 0.42$ ). Here, we aim to test this prediction at the catchment-scale using field data and repeat observations surrounding storms.

## 4 | STUDY SITES FOR TESTING THE THRESHOLD HYPOTHESIS

### 4.1 | Overview of San Gabriel Mountains and northern San Jacinto Mountains, southern California

The SGM and NSJM are two steep, rocky mountain ranges with similar crystalline bedrock lithology and semi-arid climate, but differing erosion rate and contrasting bedrock fracture density (Figure 1; DiBiase et al., 2018). Bedrock in both landscapes primarily consists of granite, granodiorite, and tonalite, with local occurrences of gneiss, schist, and marble (Jennings et al., 1977). In steep catchments of the SGM and NSJM, there is a patchwork of soil-mantled slopes and steep bedrock cliffs that supply coarse sediment to colluvial channels (Neely et al., 2019; Neely & DiBiase, 2020). Channel floors in both landscapes have occasional bare-bedrock steps but are otherwise covered by a nearly continuous mantle of cobble to boulder-sized bed sediment supplied from steep rocky hillslopes. Channel walls are confined by steep hillslopes and bedrock walls, and large woody debris is sparse in channels.

Detrital  $^{10}\text{Be}$ -derived erosion rates from stream sands in the SGM range from 0.036 to 2.2 m  $\text{kyr}^{-1}$  and are 2–5× higher than the range

of erosion rates of 0.04 to 0.61 m  $\text{kyr}^{-1}$  for watersheds of similar morphology in the NSJM (DiBiase et al., 2010; DiBiase et al., 2018; Heimsath et al., 2012; Neely et al., 2019). Mean hillslope angles generally increase with catchment averaged erosion rates in both landscapes, and above mean hillslope angles of  $\sim 35^\circ$ , hillslope steepening is accommodated by increasing exposure of bare-bedrock cliffs as erosion rates increase (Neely et al., 2019).

We leverage similar bedrock lithology, topography, and hydrologic forcing, but starkly different bedrock fracture spacing and sediment grain size between the SGM and NSJM to isolate connections between sediment grain size and steep channel morphology. Relative to the NSJM, the SGM have 5× greater bedrock fracture density and  $\sim 3\times$  finer surface sediment grain size (Neely & DiBiase, 2020).

### 4.2 | Historic observation of sediment motion in SGM and NSJM steep channel networks

Historical records gathered from local reports and gaging stations indicate that major floods or debris flows occur over approximately decadal recurrence intervals in the SGM and NSJM (National Weather Service, 2017; Scott, 1971; Wells, 1982). Some of the most destructive debris flows in southern California occur following wildfires that change catchment hydrology and sediment dynamics such that rainfall thresholds for triggering debris flows are reduced (Staley et al., 2020). However, the impact of wildfire on sediment flux is typically limited to the first few years following a burn, and the longer-term impacts of wildfire on sediment cover and channel incision are not well understood (Lamb et al., 2011; Rengers et al., 2021). We restrict our analysis to locations that have not been affected by wildfire for at least 10 years, and thus assume hillslopes and channels have recovered from such disturbances.

Over the last decade, the region has been covered by repeat surveys of 6–17-cm/pixel high-resolution resolution imagery (Pictometry Corp.; <https://www.eagleview.com/product/pictometry-imagery/>), which permits more detailed mapping of sediment motion throughout the steep channel networks. Surface sediment grain size in the NSJM is coarse enough that  $D_{50}$ -sized sediment in the channel network is resolved and repeat imagery can be used to directly compare movement of sediment to historic discharge records. In the SGM, sediment sizes are generally too fine to resolve in 6–17-cm resolution imagery, limiting analysis to the mapping of freshly-scoured channels.

Between two sets of imagery collected in the NSJM, an atmospheric river event from February 14–15, 2019, triggered widespread flooding and debris flows in Chino Canyon and Snow Creek (Figure 4; Hatchett et al., 2020). Two-day rainfall totals of 22.4 cm and 22.9 cm were recorded at the Mount San Jacinto Ranger Station (elevation 2626 m) and Snow Creek Idyllwild (elevation 1691 m) rain gages, respectively. At the mouth of Chino Canyon (elevation 709 m,  $A = 10 \text{ km}^2$ ), a debris flow damaged the Palm Springs Aerial Tramway building and overtopped the banks of a 3–5-m deep channel, leading to a shallow overspill avulsion upstream from the Tramway building.

Between repeat imagery and lidar surveys in the eastern SGM, a suite of debris flows occurred between February 2014 and a June 2015 airborne lidar survey that resolved widespread channel scour (DiBiase & Ferrier, 2020). Debris flows visible in 2017 imagery data occurred on steep slopes near Mount Baldy and Icehouse Canyon,

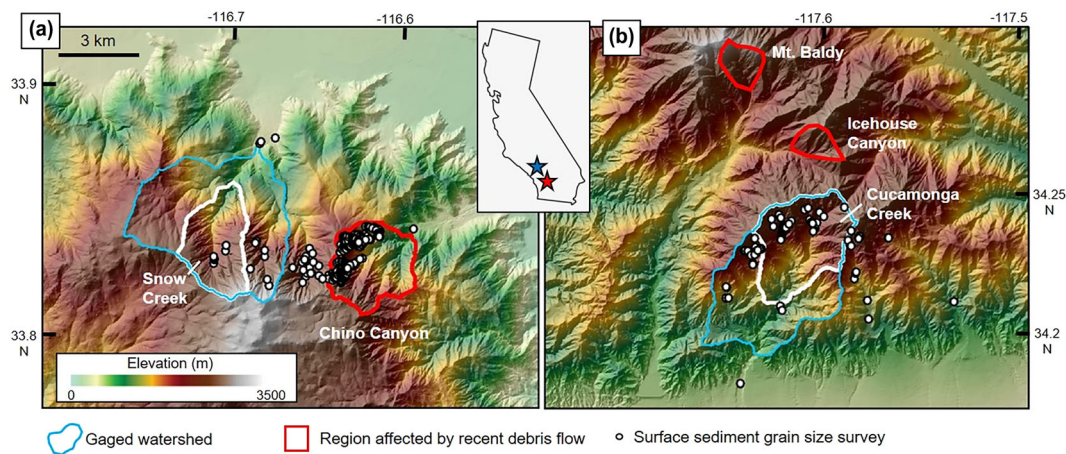


**FIGURE 4** Maps of (A) northern San Jacinto Mountains and (B) San Gabriel Mountains showing focused study catchments of Snow Creek and Cucamonga Creek upstream from stream gages (cyan outline) and where headwater catchment topography was quantified (white outline). Red outlines indicate neighboring regions where recent debris flows were mapped from repeat aerial imagery (Figure 9). Inset map shows location of landscapes within California, USA. Sediment grain size data are from Neely & DiBiase (2020) [Color figure can be viewed at [wileyonlinelibrary.com](https://wileyonlinelibrary.com)]

California ( $A < 2 \text{ km}^2$ ) but flows did not reach the range front of the SGM. The largest storm rainfall total observed over this time period was 6.3 cm and occurred during February 27–28, 2014 measured at the Tanbark weather station in the San Dimas Experimental Forest, which lies  $\sim 10$  km west of the location of observed debris flows (<https://www.wrh.noaa.gov/map/>).

## 5 | METHODS FOR DOWNSTREAM ANALYSIS IN SGM AND NSJM

### 5.1 | Approach for field data synthesis

To estimate the extent and style of sediment entrainment in the SGM and NSJM headwater channel networks, we computed the flow depth and bed shear stresses needed to mobilize the  $D_{50}$  size-class of bed sediment using the framework described in Section 3. We used empirical relationships constructed from field data to constrain the drainage-area dependence of channel gradient (Section 5.2.1), channel width (Section 5.2.2), channel bank angle (Section 5.2.3), sediment grain size (Section 5.2.4), and discharge (Section 5.3). We calculated the water discharge and flow depth required for  $D_{50}$  motion and flood sizes of various recurrence intervals at 50 logarithmically spaced nodes between drainage areas of 0.001 and  $30 \text{ km}^2$  in representative catchments of both landscapes using Equations (4)–(13). Flood sizes and recurrence intervals were constrained by analysis of historic streamflow records across the SGM and NSJM (Section 5.3). We also inferred downstream patterns in rock compressive strength from Schmidt hammer rebound values measured from hillslope outcrops and in-channel bedrock steps (Section 5.2.5).

From each landscape, we focused our analysis on one steep watershed where field measurements overlap (Figure 4, see also Figure S3). In the SGM, Cucamonga Creek contains a dense array of sediment grain size surveys,  $^{10}\text{Be}$  erosion rates, and a stream gage at the outlet of the catchment that operated from 1925 to 1975 water years (US Geological Survey [USGS] gaging station number 11073470, drainage area =  $25 \text{ km}^2$ ). In the NSJM, Snow Creek contains a similar array of field measurements and a stream gage that has

operated from the 1960 water year to present (USGS gaging station number 10256500, drainage area =  $28 \text{ km}^2$ ). We include sediment grain size surveys from neighboring catchments with similar topography and erosion rates to define downstream sediment grain size sorting trends (Neely et al., 2019; Neely & DiBiase, 2020).

### 5.2 | Constraints on channel geometry and bed material grain size

#### 5.2.1 | Channel slope

Following methods described in Section 2, we applied the empirical fit of Equation (1) to downstream changes in channel slope extracted from topographic datasets derived from airborne lidar surveys spanning Snow Creek in the NSJM and Cucamonga Creek in the SGM (DiBiase & Ferrier, 2020). We focused topographic analysis on one subcatchment from each site where channel morphology across tributaries is most uniform and colluvial channels are predominately sediment mantled (Figure 4). A drainage area of  $10^3 \text{ m}^2$  was used to define the upstream extent of the colluvial channel network and incorporate the extent of channel width and sediment grain size surveys throughout colluvial channels.

#### 5.2.2 | Channel width

We measured the basal channel width,  $w_b$ , at 175 bedrock channel locations in the NSJM and 238 bedrock channel locations in the SGM using high-resolution orthophotos derived from commercial aerial imagery and published uncrewed aerial vehicle (UAV) imagery surveys (Pictometry Corp.; <https://www.eagleview.com/product/pictometry-imagery/>; Carr et al., 2021) (see Figure S3). Basal channel width was measured between two bedrock banks and identified by base streamflow visible in imagery at larger drainage areas ( $> 5 \text{ km}^2$ ). At drainage areas less than  $1\text{--}2 \text{ km}^2$  in the SGM and NSJM, channel bottoms are typically dry, but have well-defined contrasts with adjacent steep hillslopes resolved by airborne lidar topography. In some

locations, we used lidar topography to help confirm imagery-based width measurements (see Figure S6). For modeling downstream trends in channel width, we fit a power law regression between basal channel width,  $w_b$ , and drainage area in each landscape:

$$w_b = k_w A^b, \quad (14)$$

where  $k_w$  and  $b$  are fit parameters (e.g., Montgomery & Gran, 2001).

### 5.2.3 | Channel bank angle

Using airborne lidar topography, we extracted channel cross-sections at each location with a basal channel width measurement to estimate bank angle in the SGM. We measured channel width at elevations of 1 m, 2 m, and 3 m above the channel thalweg to span flow depths observed in channels over historic timescales and measure bank angles relative to basal channel width,  $w_b$ . The mean bank angle is approximately 40° for each height above the channel thalweg, and there is no systematic downstream change in bank angle (see Figure S7). We assumed a constant bank angle,  $\alpha = 40^\circ$ , which is similar to mean hillslope gradients measured in each landscape (DiBiase et al., 2012; Neely et al., 2019).

### 5.2.4 | Sediment grain size

Surface sediment grain sizes in the SGM and NSJM were compiled from previous work combining field and remote sensing approaches (Neely & DiBiase, 2020). Surveys typically represent the surface

**TABLE 1** Parameter values used to calculate flow depths and threshold flow depths of  $D_{50}$  motion.

Parameter	Snow Creek (northern San Jacinto Mountains)	Cucamonga Creek (San Gabriel Mountains)
$S_0$	0.76	0.76
$a_1$	$0.67 \text{ km}^{-1.22}$	$1.5 \text{ km}^{-1.06}$
$a_2$	0.61	0.53
$k_w$	$0.77 \text{ m}^{0.07}$	$0.87 \text{ m}^{0.06}$
$b$	0.14	0.12
$k_{c50}$	0.27	0.24
$k_{f50}$	0.38	0.35
$k_{c84}$	0.32	0.28
$k_{f84}$	0.51	0.21
$D_{50\max}$	1.2 m	0.34 m
$D_{84\max}$	4.1 m	0.97 m
$R_{3,10,20}$	$0.037, 0.152, 0.285 \text{ m d}^{-1}$	$0.041, 0.136, 0.439 \text{ m d}^{-1}$
$Fa_1$	$6.5^\dagger$	$6.5^\dagger$
$Fa_2$	$2.5^\ddagger$	$2.5^\ddagger$
$C_1$	$0.19^\ddagger$	$0.19^\ddagger$
$C_2$	$0.34^\ddagger$	$0.34^\ddagger$
$\alpha$	$40^\circ$	$40^\circ$

<sup>†</sup>After Ferguson (2007).

<sup>‡</sup>After Prancevic & Lamb (2015b).

sediment grain size across the entire valley floor, particularly in colluvial hollows where channel banks are not always clearly defined when full of colluvium (Figure 1D, E). We compiled 84 and 180 individual surveys in the SGM and NSJM, respectively. The individual surveys consist of 40–674 clasts each and typically cover reach lengths that are 2–20× the basal channel width.

Sediment grain size measurements in the NSJM and SGM were made using aerial imagery and field surveys collected either prior to large storms or in sites unaffected by observed debris flows in the SGM. Due to the large spatial region encompassed by all field surveys in each landscape, we assume that sediment grain size patterns measured in each landscape reflect long-term ( $>10^2$ – $10^3$  years) sediment delivery from hillslopes to channels and not transient patterns of sediment deposition from a single recent storm event or landscape disturbance such as fire.

To model downstream changes in surface sediment grain size across each landscape, we fit an empirical relationship to a pattern of downstream coarsening at low drainage areas and a pattern of downstream fining at larger drainage areas, which is observed in both sites (Neely & DiBiase, 2020). We focused on the  $D_{50}$  (median) and  $D_{84}$  grain size fractions, which are commonly used to parameterize sediment transport and flow hydraulics (Equations 4–13). We relied on the large number of individual surveys to define downstream trends, which can be obscured if small sample sizes are used due to spatial and temporal variation in local hillslope sediment delivery (Marc et al., 2021; Roda-Boluda et al., 2018) or varying accuracy of sediment size measurements on both scaled imagery and orthoimagery (Mair et al., 2022). We calculated the mean  $D_{50}$  and  $D_{84}$  for 10 logarithmically-spaced bins of drainage area from  $0.001 \text{ km}^2$  to  $30 \text{ km}^2$ . The inflection between systematic downstream coarsening and systematic downstream fining,  $A_{cD}$ , is defined as the geometric mean of the drainage-area-bin endpoints for the log-bin with the coarsest mean grain size ( $D_{50\max}$  and  $D_{84\max}$ ). We then fit a piecewise power-law fit to all survey points for drainage areas less than and greater than  $A_{cD}$ :

$$D_{50,84}(A) = \begin{cases} D_{50\max,84\max} \left(\frac{A}{A_{cD}}\right)^{k_{c50,84}}, & \text{for } A \leq A_{cD} \\ D_{50\max,84\max} \left(\frac{A}{A_{cD}}\right)^{-k_{f50,84}}, & \text{for } A > A_{cD} \end{cases}, \quad (15)$$

where  $k_{c50,84}$  and  $k_{f50,84}$  are exponents describing the rate of downslope coarsening and downslope fining, respectively.

### 5.2.5 | Rock strength from Schmidt hammer rebound surveys in the SGM and NSJM

In the SGM and NSJM, we used a Proceq Rock-Schmidt, Type-N 20–150 MPa Schmidt hammer to approximate the compressive strength of the *in situ* rock mass on hillslope outcrops and bedrock steps within the channel network from drainage areas of 0.001–30 km<sup>2</sup>. At each hillslope outcrop or in-channel bedrock site (5–10 m<sup>2</sup> area each), we measured sets of 20 individual rebound values on three to five ~2–3 m<sup>2</sup> patches. Impact measurements were made at approximately 25 cm spacing and avoided bedrock fractures.

### 5.3 | Historical streamflow analysis

We used historical streamflow data to define magnitude–frequency distributions of water discharge,  $Q$ , as a function of drainage area,  $A$ , and to compare with our model predictions of flow depth. In the SGM, we analyzed streamflow records from 17 stream gages that range in drainage area from 0.3 to 200 km<sup>2</sup> and operated synchronously over the 1939–1959 water year period. Peak annual runoff ( $Q/A$ ) varies minimally with drainage area for floods with  $\sim 3$ ,  $\sim 10$ , and  $\sim 20$ -year recurrence intervals (see Figure S4), suggesting that an approximately linear relationship between peak discharge and drainage area extending to drainage areas as small as 0.3 km<sup>2</sup>, consistent with prior analyses (DiBiase & Whipple, 2011; Lavé & Burbank, 2004).

In the NSJM, we used a 69-year record of peak annual discharges measured at Snow Creek (USGS station 10256500). The February 2019 storm (Hatchett et al., 2020) that triggered debris flows in Chino Canyon and Snow Creek was the third largest peak annual discharge on record over this time interval corresponding to a recurrence interval of 23 years. We assume that a linear relationship between peak annual discharge and drainage area also applies to the NSJM due to the similarity of runoff patterns between the SGM and NSJM (DiBiase et al., 2018). To estimate peak flow depths for comparison to our runoff model (Equations 6–10), we compared stage height data from  $\sim 3$ ,  $\sim 10$ , and  $\sim 20$ -year recurrence interval floods at Snow Creek and Cucamonga Creek to stage height at low or no flow (see Figure S5).

### 5.4 | Mapping sediment motion with repeat imagery

Using repeat imagery, we compared measured channel geometries and predicted incipient motion thresholds to the width of observed erosive events and, where possible, the motion of individual clasts. In Snow Creek, we used streamflow data and orthoimages from

December 2012, June 2015, and January 2020 to identify motion of streambed sediment coarser than 50-cm diameter in the NSJM, which corresponds to approximately the  $D_{50}$  grain size of NSJM channel sediment. Between each set of orthoimages, we visually assessed the movement of sediment coarser than 50 cm in 200-m long channel reaches spanning from 0.1 to 25 km<sup>2</sup> in the Snow Creek watershed. Snow cover obscured observations from above elevations of  $\sim 1800$  m in the January 2020 imagery set. Motion of  $D_{50}$  sediment between image sets was recorded if  $D_{50}$ -sized clasts either left or arrived within the 200-m channel reach (fluvial transport) or if riparian vegetation was removed (e.g., Church & Jakob, 2020). We thus define motion by travel distances of tens of meters and ignore shifting or rotation at smaller scales. We also used repeat aerial imagery to map downstream changes in the width of flows that occurred during recent storms with repeat imagery. At approximately 100-m intervals, we measured flow width between newly-constructed debris flow levees where present.

## 6 | RESULTS

### 6.1 | Downstream changes in channel geometry, sediment grain size, and rock strength

#### 6.1.1 | Downstream changes in channel slope

In the SGM and NSJM, downstream changes in headwater channel gradient are well described by the empirical relationship of Stock & Dietrich (2003) (Figure 5A; Equation 1). Colluvial channels show a similar maximum channel gradient, with  $S_0$  values of 0.76 for both Cucamonga Creek and Snow Creek. However,  $A_{cs}$ , the drainage area at which colluvial channels transition to longitudinally concave channels, varies by  $\sim 4\times$ , from 0.5 km<sup>2</sup> in Cucamonga Creek in the SGM to 1.9 km<sup>2</sup> in Snow Creek in the NSJM (Figure 5A).

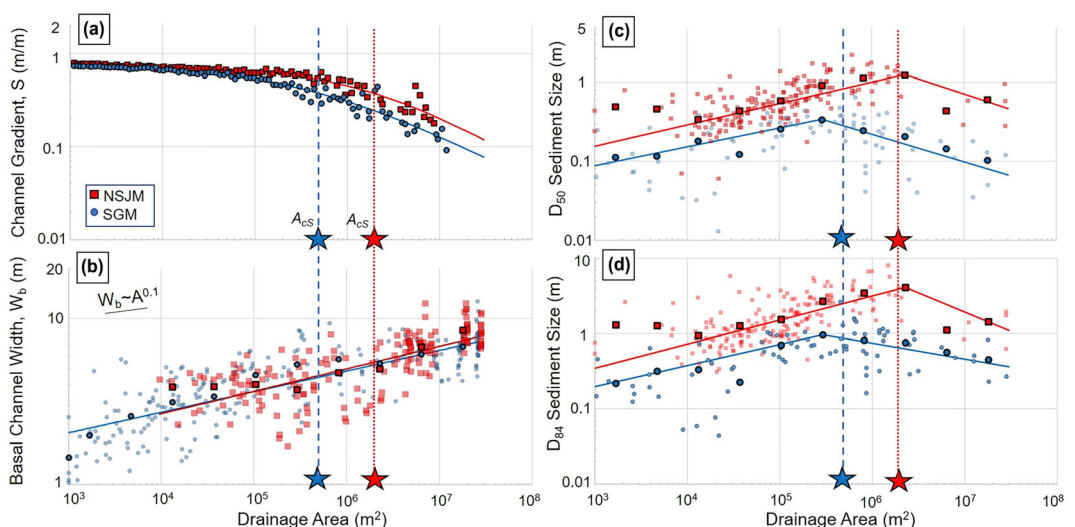


**FIGURE 5** Downstream changes in (A) channel slope, (B) basal channel width, and (C, D) surface sediment grain size in the northern San Jacinto Mountains (NSJM) and San Gabriel Mountains (SGM). Stars and vertical dashed lines delineate  $A_{cs}$ , the drainage area where channel morphology transitions from near-constant gradient colluvial channels to concave-up fluvial channels in both landscapes. Regressions in (B), (C), and (D) were fit to individual data points (transparent symbols). Log-binned averages (solid symbols) were used to fit slope–area data in (A) and identify the transition from downstream coarsening to downstream fining,  $A_{cd}$  (C) (Table 1) [Color figure can be viewed at [wileyonlinelibrary.com](http://wileyonlinelibrary.com)]

## 6.1.2 | Downstream changes in basal channel width

In both sites, basal channel width increases similarly downstream as a power law function of drainage area (Figure 5B); however, the exponent is smaller ( $b \sim 0.1$ ) than typically observed in compilations that compare channel width and drainage area in larger fluvial rivers, where  $b$  ranges from 0.3 to 0.5 (Lague, 2014). In general, headwater channels at small drainage areas ( $< 1 \text{ km}^2$ ) are 2–5× wider than expected relative to channel width scaling relationships estimated from fluvial rivers with larger drainage areas (Whipple et al., 2022).

## 6.1.3 | Downstream changes in sediment grain size

The transition from downstream coarsening to downstream fining occurs at a similar drainage area as the change in longitudinal channel geometry from constant-gradient channels to concave-up channels, with  $A_{cD} \sim 0.3 \text{ km}^2$  in the SGM and  $A_{cD} \sim 2 \text{ km}^2$  in the NSJM (Figure 5). Despite large differences in overall sediment size, the rates of downslope coarsening with increasing drainage area are similar between the SGM ( $k_{c50} = 0.24$ ;  $k_{c84} = 0.28$ ) and NSJM ( $k_{c50} = 0.27$ ;  $k_{c84} = 0.32$ ), with slightly more rapid downslope coarsening of the  $D_{84}$  size fraction than the  $D_{50}$ . Downslope fining trends show more scatter and less correspondence between the SGM ( $k_{f50} = 0.35$ ;  $k_{f84} = 0.21$ ) and NSJM ( $k_{f50} = 0.38$ ;  $k_{f84} = 0.51$ ); however, fewer surveys are available in the NSJM ( $N=8$ ) to constrain downslope fining trends due to difficulty accessing this portion of the channel network.

## 6.1.4 | Downstream changes in intact rock strength

In each landscape, Schmidt hammer rebound values ( $R$ ) increase moving downstream through the headwater channel network by 10–20  $R$ , beginning at 50–60  $R$  at the upslope extent of colluvial channels and

reaching maximum values of 70–80  $R$  at the downstream-most survey sites (Figure 6). Schmidt hammer rebound values on all bedrock channel steps are similar between the NSJM and SGM, with mean and 1 $\sigma$  of all channel step rebound values of  $59 \pm 14 \text{ R}$  and  $63 \pm 14 \text{ R}$  respectively (Figure 6). The mean rebound values of all bedrock outcrops are lower than rebound values on in-channel bedrock steps, and NSJM bedrock outcrops ( $44 \pm 16 \text{ R}$ ) are lower than SGM bedrock outcrops ( $55 \pm 14 \text{ R}$ ).

## 6.2 | Predicted thresholds of mobilization by fluvial and debris flow processes

### 6.2.1 | Modeled critical flow depths for fluvial entrainment

For each landscape, the predicted critical flow depth for fluvial initial motion of  $D_{50}$  bed sediment increases with increasing drainage area until the switch from downstream coarsening to downstream fining at  $A = A_{cD}$ , which also occurs near the slope-area scaling break of  $A_{cS}$  (Figure 7). The critical flow depth is mainly sensitive to surface sediment grain-size patterns within and between landscapes, with the highest predicted critical flow depths in the NSJM and lower critical flow depths in the SGM. In both landscapes, the critical flow depth for fluvial transport is mostly only exceeded at larger drainage areas  $A > A_{cD}$  for the modeled discharge recurrence intervals. Despite decreased surface sediment grain size at low drainage areas, the relative invariance of slope and width leads to predicted flow depths that are 2–10× below critical in colluvial channels ( $A < A_{cD}$ ) of the SGM and NSJM during discharges with decadal recurrence intervals. Although predicted flow depths match observations of clearwater flows at gaging stations, measurements of peak flow depths from debris flow surges in the SGM and NSJM are significantly higher (Figure 7), indicating the importance of debris flows for mobilizing coarse sediment in colluvial channels.

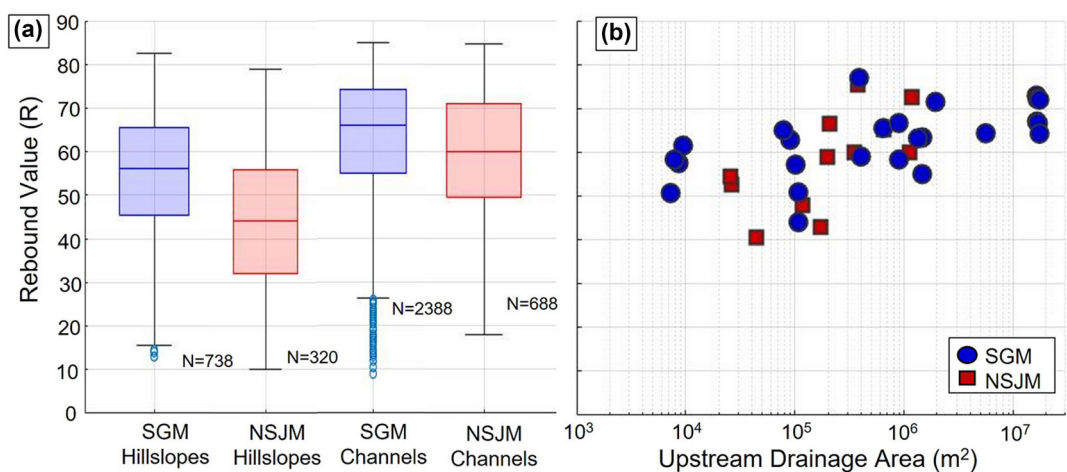


**FIGURE 6** (A) Summary boxplots of all Schmidt hammer rebound values by landscape position in the San Gabriel Mountains (SGM) and northern San Jacinto Mountains (NSJM). Boxes record median, upper and lower quartiles. Whiskers extend from quartiles and are 1.5× the interquartile range. Circles denote outliers exceeding whisker lengths.  $N$  denotes total number of impact measurements. (B) Downstream pattern in mean Schmidt hammer rebound value recorded on bedrock channel steps in both landscapes. Symbols indicate the mean of 1–5 individual surveys (with 20 impact measurements each) at each location [Color figure can be viewed at [wileyonlinelibrary.com](https://wileyonlinelibrary.com)]

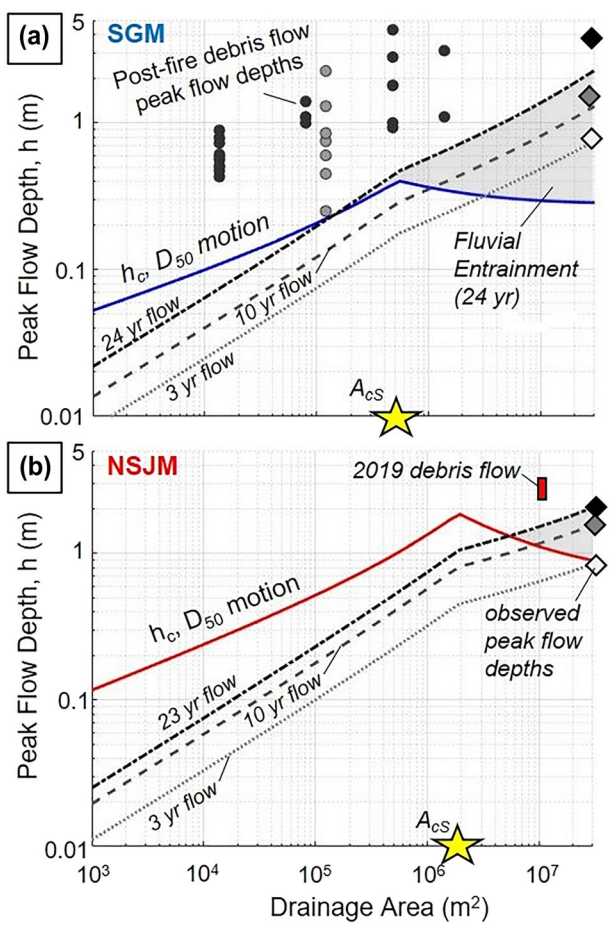


**FIGURE 7** Solid colored lines show flow depth required to mobilize  $D_{50}$  bed sediment according to critical shields criterion for fluvial entrainment in (A) Cucamonga Creek, San Gabriel Mountains (SGM) and (B) Snow Creek, northern San Jacinto Mountains (NSJM). Gray shading highlights drainage areas where bed sediment motion by fluvial entrainment is predicted during discharges with  $\sim 20$ -year recurrence intervals. Peak flow depths measured at gaging stations are marked with diamonds for flood sizes of  $\sim 3$ ,  $\sim 11$  and  $\sim 20$ -years, and corresponding dashed lines show modeled flow depths upstream. Circles show peak debris flow surge heights observed at monitoring stations in nearby headwater channel systems in the SGM (Kean et al., 2011, dark gray; Tang et al., 2019, light gray), and in video surveillance of the Palm Springs Aerial Tramway during the 2019 Chino Canyon debris flow in the NSJM (approximated by red box), [https://www.youtube.com/watch?v=v3g\\_E6OfS8](https://www.youtube.com/watch?v=v3g_E6OfS8) [Color figure can be viewed at [wileyonlinelibrary.com](http://wileyonlinelibrary.com)]

### 6.2.2 | Modeled downstream patterns in sediment mobility accounting for both fluvial and debris flow initial motion

In colluvial channels of both landscapes, bed sediment transport is predicted to occur by mass wasting of the channel bed for peak flows with  $\sim 20$ -year recurrence intervals (Figure 8). For the NSJM, there is a gap at the colluvial-fluvial transition where no transport (either debris flow or fluvial) is expected, which arises primarily due to the peak in bed-sediment grain size occurring at fluvial channel heads (Figure 4C; Neely & DiBiase, 2020). In both the SGM and NSJM, fluvial transport is predicted downstream of  $A_{CS}$ , which generally corresponds to  $A_{CD}$ , the transition from downstream coarsening to downstream fining (Figure 8). Fluvial transport stage ( $\tau/\tau_{cf}$ ) continues to increase moving downstream from  $A_{CS}$ .

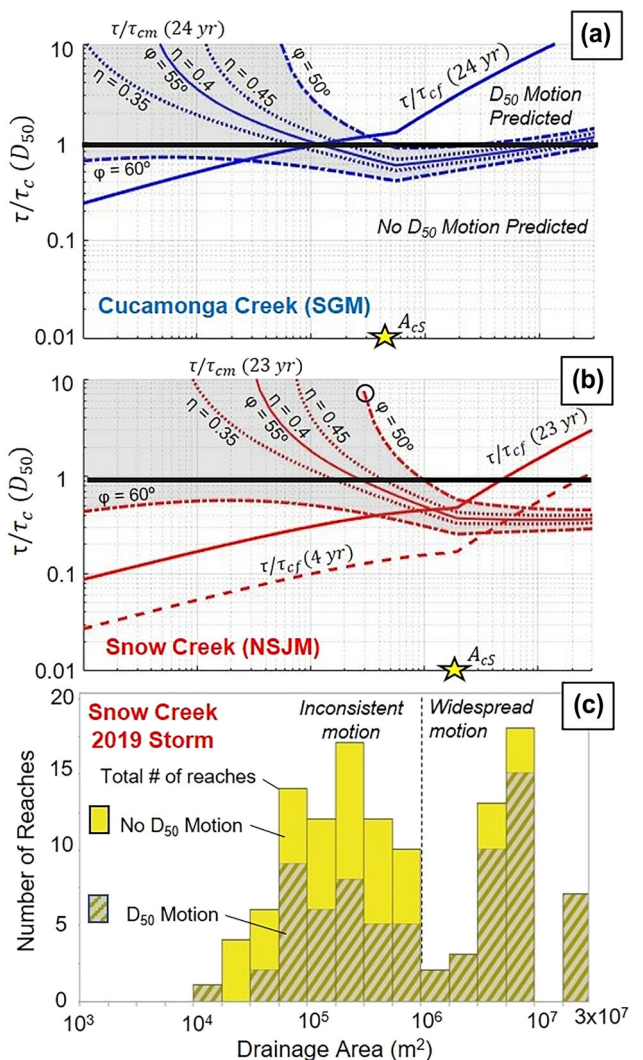


**FIGURE 8** Plots showing ratio of modeled bed shear stress and critical bed shear stress for  $D_{50}$  motion by fluvial entrainment ( $\tau/\tau_{cf}$ ) and bed failure by mass wasting ( $\tau/\tau_{cm}$ ) in (A) Cucamonga Creek and (B) Snow Creek. Shaded areas in (A) and (B) reflect  $\tau/\tau_{cm}$  for a range of parameter values for Equation (12) used by Prancevic et al. (2014):  $\varphi = 55 \pm 5^\circ$ ,  $\eta = 0.4$  (dot-dashed lines);  $\varphi = 55$ ,  $\eta = 0.4 \pm 0.05$  (dotted lines). Certain combinations of  $\varphi$  and  $\eta$  are frictionally unstable across portions of the colluvial channel network during dry conditions (open circle). (C) Downstream patterns of  $\sim 100$  m long reaches in Snow Creek where  $D_{50}$  sized sediment was mobilized (hatched) or not mobilized (solid) during 2019 storm with 23-year discharge recurrence interval. No motion was observed in Snow Creek during the period 2012–2015, where the largest peak flow had a 4-year recurrence interval [Color figure can be viewed at [wileyonlinelibrary.com](http://wileyonlinelibrary.com)]

### 6.3 | Observations of sediment motion between repeat aerial imagery in the NSJM and SGM

Three sets of high-resolution repeat aerial photographs from the NSJM constrain the critical discharge for  $D_{50}$  mobilization to floods with recurrence intervals between 4 and 23 years. No significant motion of  $D_{50}$ -sized sediment was observed between 2012 and 2015 in the channel network of Snow Creek (Figure S8). The largest peak annual discharge recorded at the Snow Creek gage (USGS gaging station number 10256500) between 2012 and 2015 photographs was  $16 \text{ m}^3 \text{ s}^{-1}$  (February 28, 2014), with a peak flow depth of 1.19 m at a drainage area of  $\sim 28 \text{ km}^2$  (recurrence interval of  $\sim 4$  years). Between

aerial photographs taken in 2015 and 2020, widespread motion of  $D_{50}$ -sized sediment was observed (Figure S8). The largest event recorded during this time interval at the Snow Creek gage was the February 14–15, 2019 storm, with a peak flow of  $90 \text{ m}^3 \text{ s}^{-1}$  and a

peak flow depth of 2.3 m at the same gaging station, corresponding to a recurrence interval of 23 years. The  $D_{50}$  motion and significant bed reworking was observed in approximately half of headwater channels with 2015 and 2020 imagery coverage in Snow Creek during the

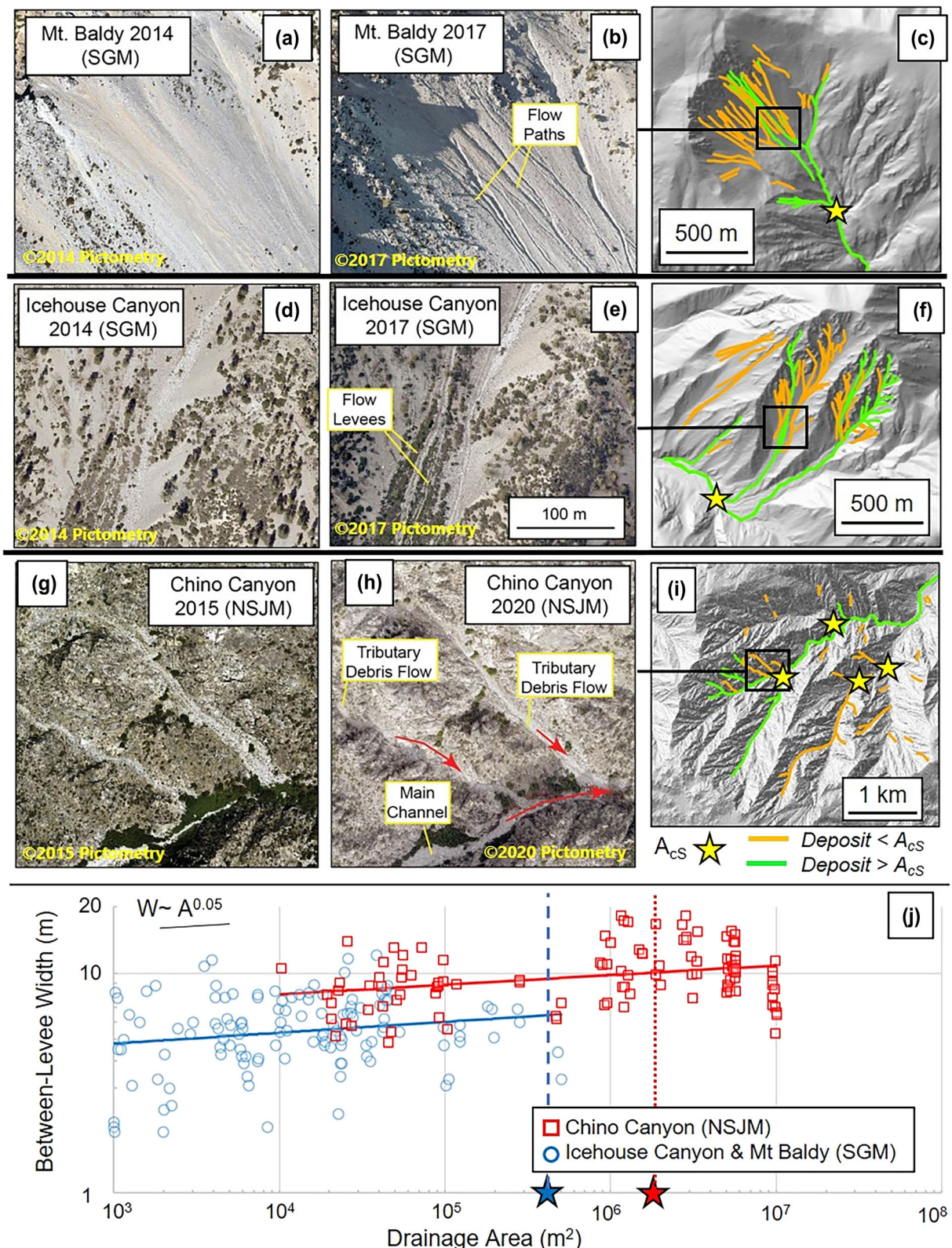


**FIGURE 9** Observations of recent debris flows in (A–C) Mount Baldy, (D–F) Icehouse Canyon, and (G–I) Chino Canyon regions. Left and middle columns show imagery prior to and following debris flows. Right column shows paths of debris flows that deposited in channels upstream of  $A_{CS}$  (orange) and downstream of  $A_{CS}$  (green). Stars in all panels represent  $A_{CS}$  of  $1.9 \text{ km}^2$  in northern San Jacinto Mountains (NSJM) and of  $0.5 \text{ km}^2$  in the San Gabriel Mountains (SGM). Debris flows occurred during winter of 2014–2015 in the SGM (A–F) and during winter of 2019 in the NSJM (G–I). Minimal downstream changes in debris flow width measured between preserved levees from these events is reported in (J) for all three sites where debris flow paths were mapped [Color figure can be viewed at [wileyonlinelibrary.com](https://onlinelibrary.wiley.com)]

February 2019 storm (Figure 8C). While some headwater channels experienced complete mobilization of the bed sediment cover, other nearby headwater channels showed no change (Figure S8). Similar patterns of sediment motion were observed in neighboring Chino Creek (Figure 9I).

Similar to the patterns observed between basal channel width and drainage area (Figure 5B), the width of channels scoured by observed debris flows increases minimally with increasing drainage area downstream ( $b = 0.05$ ) in both the SGM and NSJM (Figure 9J). Flows in the eastern SGM 2014–2015 Icehouse Canyon and Mount Baldy event left clear debris flow levees that terminate at drainage areas between 0.5 and 2 km<sup>2</sup>. In the NSJM 2019 event, consistent debris-flow-levees were preserved following a debris flow that was observed in video surveillance at the Palm Springs Aerial Tramway at the base of Chino Canyon (drainage area ~10 km<sup>2</sup>), east of Snow Creek. As seen with basal channel widths ( $w_b$ ), freshly-scoured channels are wider than expected at small drainage areas when compared to drainage area-width scaling relationships typically applied to larger rivers ( $b \sim 0.3\text{--}0.5$ ).

## 7 | DISCUSSION

### 7.1 | Implications for colluvial channel form and process

Our initial motion model predicts that in-channel bed failure is a primary mechanism for mobilizing sediment on decadal timescales in colluvial channels ( $A < A_{CS}$ ) of the SGM and NSJM (Figure 8). Even for larger storms, peak stream flows are insufficient to mobilize bed sediment by fluvial entrainment in these steep, constant gradient channels. This behavior arises mainly because of steep gradients ( $S > 0.7$ ) but is also facilitated by wide channels that limit the predicted depth of overland flow in colluvial channels (Figures 5B and 9J). The similarity of basal channel-width scaling in colluvial channels with the width of recent debris flows additionally points to the importance of debris flows for setting channel width in colluvial channels.

Our model predictions of channel bed failure agree with observations of debris flow scour throughout headwater channel networks from repeat aerial imagery in the SGM and NSJM (Figure 9). Debris flows traversed across 47% of all colluvial channel reaches ( $A < A_{CS}$ ) and flows either terminated near the base of colluvial channels or traversed downstream to lower gradient channels ( $S < 0.1$ ) (Figures 8 and 9). Spatial variability in debris flow nucleation between neighboring channels may reflect spatial differences in headwater catchment hydrology (Rossi et al., 2020) or bed porosity and the internal angle of frictional stability within colluvial material (Prancevic & Lamb, 2015a; Zimmermann et al., 2010), which can have strong effects on the stability of bed sediment through colluvial channels (Figure 8). Spatially variable nucleation of debris flows between neighboring channels is also consistent with varying amounts and ages of colluvial sediment fill in the SGM and elsewhere in the western United States (Campbell, 1986; Reneau et al., 1990). Additionally, in-channel bedrock steps show increasing Schmidt hammer rebound values when moving downstream throughout the colluvial channel network, possibly reflecting more extensive weathering at sites with lower drainage

area and fewer upstream debris flow sources (e.g., Murphy et al., 2016; Stock & Dietrich, 2006).

Although the channel bed failure model depends on sediment grain size (Equation 13),  $\tau_{cm}^*$  decreases with increasing slope angle, which is ultimately limited by the dry frictional stability of channel bed material (Prancevic et al., 2014). As a result, the colluvial threshold gradient,  $S_0$ , is predicted to become increasingly insensitive to the depth-normalized grain size,  $D_{50}/R$ , as sediment coarsens and slopes steepen (Figure 10). Additionally, the threshold channel model predicts the similarity in maximum colluvial channel gradient observed in the SGM and NSJM despite large differences in grain size, sediment supply, and erosion rate (Neely et al., 2019; Neely & DiBiase, 2020), supporting an interpretation that in steep colluvial channels  $S \sim S_0$  (Equation 3) (Figures 3A, 5A, and 10). In localities with resistant rock units and widespread bedrock channel segments, local colluvial channel gradient may exceed the dry frictional stability of bed material and  $S_0$ , and instead reflect the strength of intact bedrock (Figure S1). The correlation between  $S_0$  and grain size seen in our compilation may result from the tendency for resistant rock units to produce coarse sediment (Figure 3B). More detailed mapping of bedrock exposure across colluvial channels is needed to distinguish the contribution of bare-bedrock channel steps towards colluvial channel relief.

In both the SGM and NSJM, we interpret the abundance of coarse sediment at the base of colluvial channels to reflect the collection of debris flow and rockfall material delivered from upstream. At the base of colluvial channels, debris flows and landslides may preferentially arrest at tributary junctions (Dahlquist & West, 2019; Li et al., 2016), and the coarsest rockfall clasts are most likely to traverse furthest downslope to the bottom of steep channels (Copons et al., 2009). In this view, the length of constant-gradient colluvial channels reflects a combination of mass-wasting processes that

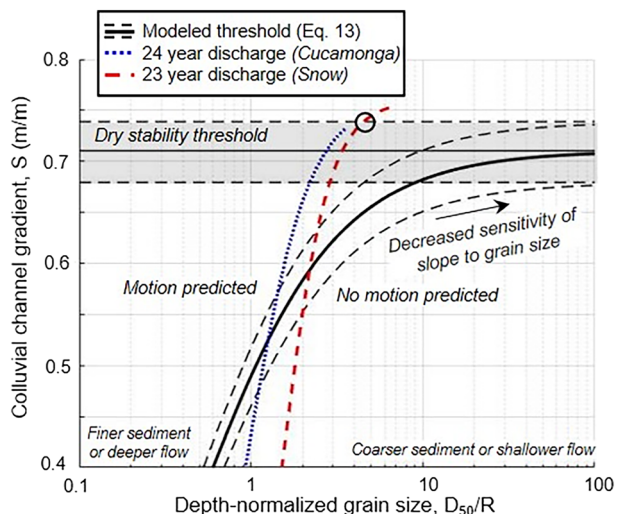


**FIGURE 10** Colluvial channel gradient sensitivity to surface sediment grain size normalized by flow depth, showing predicted threshold gradient for bed failure by mass wasting (Equation 13). Discharges with ~20-year recurrence interval for Cucamonga Creek and Snow Creek are shown, which exceed motion thresholds across steep colluvial channels. Model parameters as in Figure 8 ( $\varphi = 55^\circ$ ,  $\eta = 0.4 \pm 0.05$ ) (dashed gray lines). Circle indicates where channel slope exceeds dry stability threshold for bed-failure model [Color figure can be viewed at [wileyonlinelibrary.com](http://wileyonlinelibrary.com)]

concentrate coarse sediment at the base of steep slopes and the frequency and the magnitude of discharge events that overcome fluvial entrainment thresholds for the accumulated coarse sediment (Figure 11).

Although our compilation across a broader suite of steep headwater catchments (Figure 3) also points to a threshold control on the slopes of colluvial channels ( $S \sim S_D$ ), two potential complications arise. First, in forested landscapes like the OCR or NCCR, root cohesion may increase sediment stability in vegetated colluvial deposits, supporting steeper colluvial channels than might be expected in unvegetated landscapes (Schmidt et al., 2001). However, we see no evidence for systematically steeper colluvial channels in forested landscapes (Figure 3A, B). Second, in regions with strong bedrock or high enough rock uplift rates, bare-bedrock chutes can be carved into cliff-dominated headwalls (see Figure S1). In our compilation, these bare-bedrock chutes are restricted to a few catchments in the NSJM and eastern SGM where hillslopes are mostly exposed bare-bedrock (Neely et al., 2019). In such landscapes, colluvial channel slopes will additionally be dependent on rock properties and likely the size and flux of rockfall-derived sediment responsible for granular erosion of bedrock. Yet, because most fluvial channel headwaters are sediment mantled and lack vegetation, a robust linkage between grain size and  $A_{cs}$  persists despite these complications.

## 7.2 | Implications for fluvial channel form and process

Fluvial entrainment of bed sediment cover is generally not predicted in decadal discharges until drainage areas increase downstream of  $A_{cs}$  and  $A_{cd}$ , where channel slopes and sediment grain size both begin to decrease. At these larger drainage areas and lower channel gradients, fluvial entrainment of  $D_{50}$ -sized sediment becomes favored over mass-wasting of the channel bed (Figure 11). The critical discharge needed to mobilize  $D_{50}$  sediment by fluvial entrainment in the NSJM matches the range of discharges constrained by the 2011–2015 (no motion), and 2015–2020 (widespread motion) intervals (Figure 8).

The entrainment threshold for sediment motion by fluvial processes is exceeded by progressively smaller discharges as drainage area increases, indicating that fluvial channel slopes become increasingly steeper than the threshold model predicts (Figure 7). We interpret this to primarily reflect the increasing importance of sediment flux in setting channel slope at larger drainage areas, such that  $S_{qs} > S_D$  (Johnson et al., 2009). It is possible that increasing strength of in-channel bedrock at larger drainage areas (Figure 6B) could lead to increasing values of  $S_E$ . We did not map any systematic patterns of increasing bedrock exposure downstream in order to explore this case (Sklar & Dietrich, 2006).

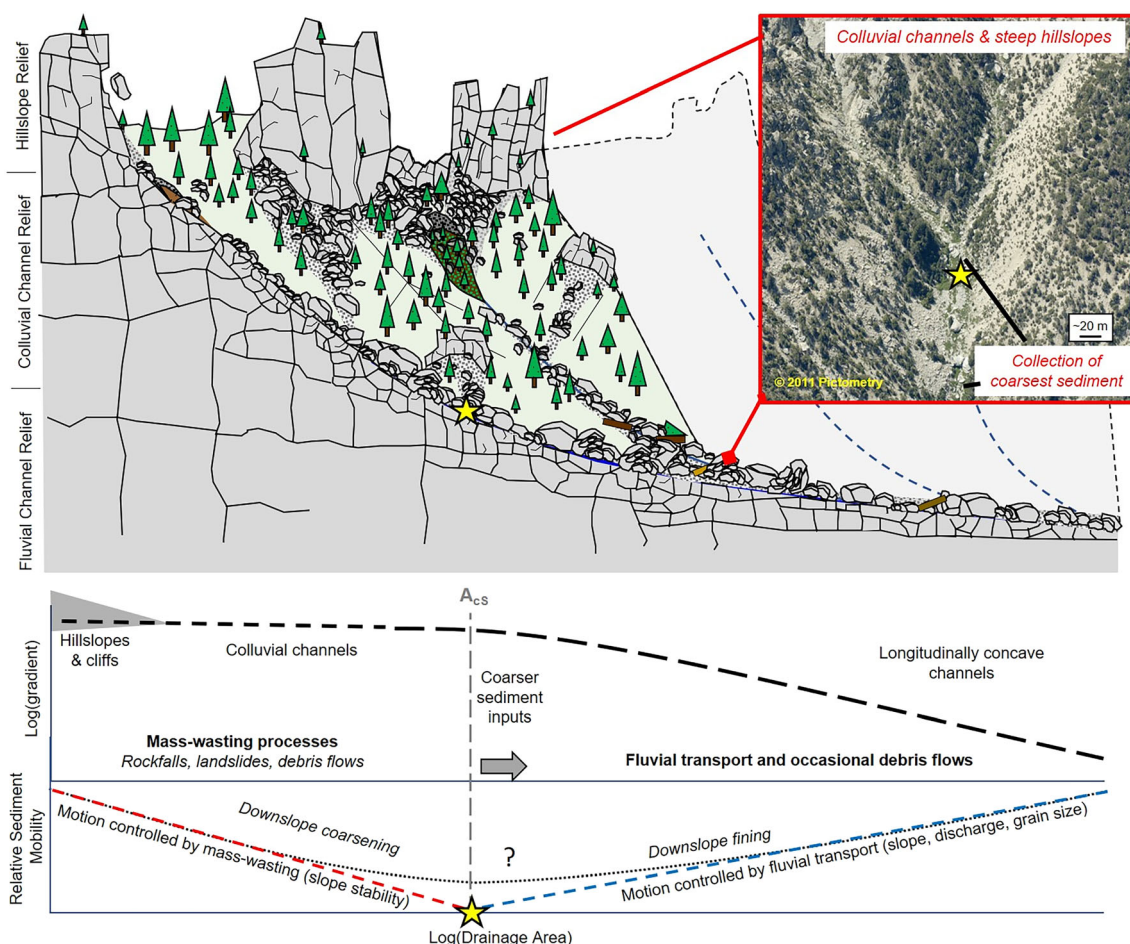


**FIGURE 11** Conceptual cartoons illustrating relationships between coarse sediment and headwater catchment morphology. Inset oblique air photograph shows transition from colluvial channel network to fluvial channel network and collection of coarse sediment (yellow star) in Snow Creek, northern San Jacinto Mountains [Color figure can be viewed at [wileyonlinelibrary.com](http://wileyonlinelibrary.com)]

From prior work, fluvial channel steepness across the NSJM and SGM ( $A > A_{CS}$ ) appears sensitive to both surface sediment grain size and  $^{10}\text{Be}$ -derived erosion rate, indicating that these fluvial channel steepness indices are not governed solely by entrainment thresholds. A grain-size-dependent fluvial incision threshold is consistent with steeper fluvial channels, coarser sediment, and slower erosion rates in the NSJM compared to the SGM (DiBiase et al., 2018). However, within the SGM, prior analysis of fluvial channels with similar sediment sizes showed that channels are steeper in regions with faster rock uplift and erosion rates (DiBiase & Whipple, 2011). Because  $S_D$  and  $S_{qs}$  are both expected to increase with grain size, and because  $S_{qs}$  and  $S_E$  are both expected to increase with increasing rock uplift and erosion rate, it is challenging to disentangle the relative contributions of each slope component of Equation (3) without additional constraints on bedload sediment flux. Additionally, although the presence of extensive bedrock exposure on hillslopes has been shown to decouple the relationship between surface sediment grain size and erosion rate (Neely & DiBiase, 2020), the total flux of sediment delivered from hillslopes to channels is expected to coarsen with increasing erosion rate (Attal et al., 2015; Sklar et al., 2017), possibly leading to an additional increase of  $S_{qs}$  with erosion rate that is related to changes in bedload sediment size. Overall, we interpret the slopes of headwater channels to reflect a shift from near-threshold dominated ( $S \sim S_D$ ) at the fluvial channel head ( $A = A_{CS}$ ), to increasingly sensitive to sediment flux and rock uplift rate at larger drainage areas (where  $\frac{\tau}{\tau_{cf}} > 1$ , Figure 8), although the partitioning of  $S_{qs}$  and  $S_E$  remains unclear.

Although debris flows reach the longitudinally-concave channel network and channels with gradients as low as 5–10%, channel morphology and bed-sediment size across these channels appear consistent with fluvial sediment transport expectations. This suggests that (1) streamflow in longitudinally-concave channels can rework bed sediment deposited from debris flows, (2) debris flows traversing longitudinally concave channels are relatively infrequent, or (3) long-term topographic signatures of debris flow and fluvial incision are similar at larger drainage areas (Stock & Dietrich, 2006).

### 7.3 | Implications for landscape evolution

The relative amount of relief accommodated by colluvial and fluvial channel networks varies substantially among steep landscapes (Figure 3E). We interpret this variation to largely reflect sediment controls on the drainage area where fluvial entrainment is favored over bed failure by mass-wasting (Figure 9, see Figure S2). With increasing erosion rate or bed sediment grain size, fluvial channels steepen in response to increasing  $S_{qs}$  or  $S_D$  towards gradients where debris flows become the dominant transport mechanism, and colluvial channel relief increases at the expense of fluvial channel relief (Figure 3). Over geologic timescales, these findings have implications for describing the total relief of steep channel networks and connecting headwater catchment morphology to regional differences in climate, tectonics, geological setting, or drainage divide mobility (Forte & Whipple, 2018; Whipple et al., 2022).

Our field measurements highlight downstream changes in intact bedrock strength, minimal downstream changes in channel width when compared to fluvial channels, and a consistent bottleneck where

the coarsest sediment accumulates at the base of colluvial channels (Figures 5, 6, and 11). All three of these trends are challenging to observe from analysis of topographic data alone and differ from empirical assumptions commonly employed in longitudinal profile analysis of channel networks. Similar downstream trends have also been observed in debris-flow prone catchment systems of the pacific northwest in the United States (Brummer & Montgomery, 2003; Montgomery & Gran, 2001; Snyder et al., 2003; Stock & Dietrich, 2006). These factors may be important considerations in debris-flow incision models that attempt to reconstruct longitudinal headwater channel profile form (McGuire et al., 2022; Stock & Dietrich, 2006).

The mobilization of coarse sediment that collects at the base of colluvial channels is generally not predicted in our model over decadal timescales (Figure 8), and likely depends on other mechanisms that we do not account for. For example, amplified runoff and fine sediment supply from hillslopes following wildfires led to elevated flow depths compared to flow dynamics assumed for clear water conditions (Kean et al., 2019; Figure 7). These flow depths may be necessary to evacuate the coarsest and least-mobile sediment, which can have sizes that approach, or even exceed, common channel widths and flow depths (Figure 5; Prancevic & Lamb, 2015a; Zimmermann et al., 2010). In similar semi-arid landscapes, wildfire dynamics may represent an important hillslope-channel coupling component that links long-term headwater channel morphology, vegetation growth, and movement of coarse sediment cover (Kean et al., 2019; Rengers et al., 2021).

## 8 | CONCLUSION

We exploited new field data to characterize downstream changes in headwater channel morphodynamics across the transition from steep, nearly constant-gradient colluvial channels to concave-up fluvial channels with lower gradients. We first explored sediment grain size and sediment flux controls on headwater channel morphology by compiling relationships among headwater channel network morphology, catchment erosion rate, and bed sediment grain size in sites across the western United States. This comparison revealed a nearly 50-fold variation in colluvial channel relief, and a 10-fold variation among landscapes with similar catchment averaged erosion rates. Colluvial relief was primarily accommodated by extending the length of steeper colluvial channels and secondarily through changes in colluvial channel gradient in catchments with extensive bare-bedrock cliff exposure. Broadly, headwater channel networks with higher topographic relief and longer colluvial channels correspond to coarser sediment grain size inputs, indicating a grain size dependent threshold of motion control on the transition from colluvial to fluvial channel incision.

We explored this hypothesis in detail by comparing the threshold of motion for bed sediment cover by fluvial entrainment and bed failure by mass wasting throughout steep headwater channel networks of the SGM and NSJM in southern California. Both landscapes contain field data to describe empirical relationships between drainage area and channel geometry, discharge, and bed sediment grain size, which is ~3x coarser in the NSJM than the SGM. Additionally, repeat aerial imagery bracketing recent storms places independent constraints on patterns of sediment motion.

Our main results show:

1. A change in sediment-transport process occurs between constant-gradient colluvial channels and concave-up fluvial channels due to different dependences between bed sediment grain size, channel slope, and whether sediment is moved by mass-wasting or fluvial entrainment.
2. Throughout constant-gradient colluvial channels, our field measurements highlight downstream changes in intact bedrock strength, minimal downstream changes in channel width when compared to fluvial rivers, and a consistent bottleneck where the coarsest sediment accumulates at the base of colluvial channels.
3. Across colluvial channels, discharges with decadal recurrence intervals are sufficient to mobilize bed sediment cover only via mass-wasting, matching observations of debris flow activity throughout a fraction of colluvial channels during recent storms.
4. Throughout concave-up fluvial channels, discharges with decadal recurrence intervals are sufficient to mobilize bed sediment cover only by fluvial processes. Additionally, entrainment thresholds are exceeded by progressively smaller discharges moving downstream through concave-up channels in both landscapes, which may reflect channel slope sensitivity to downstream increases in sediment flux.

While maximum colluvial channel gradients remain similar, the length of colluvial channels increases with increasing sediment grain size between the SGM and NSJM and across a broader compilation of steep headwater channel networks that span a range of erosion rates and geologic settings. We interpret the transition from colluvial to fluvial longitudinal profiles to reflect grain size dependent incision thresholds, where sediment transport by mass-wasting and fluvial entrainment exhibit different sensitivity between sediment grain size and channel slope. Across steep colluvial channels, channel slope appears relatively insensitive to changes in sediment size, consistent with initiation of motion thresholds for mass-wasting of the channel bed. The downstream transition from colluvial to fluvial channels appears set by fluvial entrainment thresholds, which directly couple channel slope and sediment grain size.

## AUTHOR CONTRIBUTIONS

ABN and RAD conceptualized the project. Funding was acquired by RAD and ABN. Methods were developed by ABN and RAD as the project evolved. ABN led data collection efforts. Computational analysis was conducted by ABN and RAD. ABN was supervised by RAD during the period of data collection. ABN wrote the initial draft. RAD and ABN revised and edited subsequent drafts together.

## ACKNOWLEDGMENTS

This work was supported by the National Science Foundation grant EAR-1608014 awarded to RAD. Fieldwork performed by ABN and Emily Loucks in the Guadalupe Mountains National Park was supported by the Scholten-Williams-Wright Scholarship in field geology, awarded to ABN. Joanmarie Del Vecchio, Perri Silverhart, Evan Greenberg, and Julia Carr assisted with fieldwork in the San Gabriel Mountains and California King Range. Discussions with Noah Snyder and Josh Roering aided in compiling analysis of headwater channel systems in the California King Range and Oregon Coast Range.

Discussions with Joshua Tremba at Riverside County Flood Control and Chris Bartsch at Palm Springs Aerial Tramway aided in analyzing sediment movement during the 2019 storm in the northern San Jacinto Mountains. Historic streamflow data from the gaging stations in small watersheds from the San Gabriel Mountains was prepared by Pete Wohlgemuth at the USDA San Dimas Experimental Forest. The authors would like to thank Doug Choudy, Jason Laird, David Herrero, and Frazier Haney of the Bearpaw Reserve for permitting access to steep terrain on Yucaipa Ridge in the San Bernardino Mountains.

## DATA AVAILABILITY STATEMENT

Aerial lidar datasets used to analyze catchment morphology and UAV-derived imagery for sediment grain size analysis are hosted by [opentopography.com](http://opentopography.com), with citations in text. Calculated topographic metrics and recalculated average erosion rates for headwater catchments in Figure 3 are available in the Supporting Information. Newly collected sediment grain size distributions presented in Figure 3 are available in the Supporting Information. Channel width measurements, Schmidt hammer data, and debris flow runout mapping from the northern San Jacinto Mountains and San Gabriel Mountains are included in the Supporting Information as tables and shapefiles.

## ORCID

Alexander B. Neely  <https://orcid.org/0000-0001-6142-2627>  
Roman A. DiBiase  <https://orcid.org/0000-0002-5347-8396>

## REFERENCES

- Attal, M., Mudd, S.M., Hurst, M.D., Weinman, B., Yoo, K. & Naylor, M. (2015) Impact of change in erosion rate and landscape steepness on hillslope and fluvial sediments grain size in the Feather River basin (Sierra Nevada, California). *Earth Surface Dynamics*, 3(1), 201–222. Available from: <https://doi.org/10.5194/esurf-3-201-2015>
- Balco, G., Stone, J.O., Lifton, N.A. & Dunai, T.J. (2008) A complete and easily accessible means of calculating surface exposure ages or erosion rates from  $^{10}\text{Be}$  and  $^{26}\text{Al}$  measurements. *Quaternary Geochronology*, 3(3), 174–195. Available from: <https://doi.org/10.1016/j.quageo.2007.12.001>
- Benda, L. (1990) The influence of debris flows on channels and valley floors in the Oregon coast range, U.S.A. *Earth Surface Processes and Landforms*, 15(5), 457–466. Available from: <https://doi.org/10.1002/esp.3290150508>
- Benda, L., Hassan, M.A., Church, M. & May, C.L. (2005) Geomorphology of steephead headwaters: The transition from hillslopes to channels. *Journal of the American Water Resources Association*, 41(4), 835–851. Available from: <https://doi.org/10.1111/j.1752-1688.2005.tb03773.x>
- Berti, M., Genevois, R., Simoni, A. & Tecca, P.R. (1999) Field observations of a debris flow event in the Dolomites. *Geomorphology*, 29(3–4), 265–274. Available from: [https://doi.org/10.1016/S0169-555X\(99\)00018-5](https://doi.org/10.1016/S0169-555X(99)00018-5)
- Binnie, S.A., Phillips, W.M., Summerfield, M.A. & Fifield, L.K. (2007) Tectonic uplift, threshold hillslopes, and denudation rates in a developing mountain range. *Geology*, 35(8), 743–746. Available from: <https://doi.org/10.1130/G23641A.1>
- Brummer, C.J. & Montgomery, D.R. (2003) Downstream coarsening in headwater channels. *Water Resources Research*, 39(10), 1294. Available from: <https://doi.org/10.1029/2003WR001981>
- Campbell, A.G. (1986) Sediment storage trends in several channels along the San Gabriel Mountain front, Southern California. MS Thesis. Colorado State University, Fort Collins, CO.
- Carr, J.C., Neely, A.B., Del Vecchio, J., Greenberg, E. & DiBiase, R.A. (2021) Steep headwater-Colluvial channels. Day Creek, San Gabriel

- Mountains CA, US: Distributed by OpenTopography. Available from: <https://doi.org/10.5069/G9F47MBX>
- Church, M. & Jakob, M. (2020) What is a debris flood? *Water Resources Research*, 56(8), e2020WR027144. Available from: <https://doi.org/10.1029/2020WR027144>
- Clubb, F.J., Mudd, S.M., Milodowski, D.T., Hurst, M.D. & Slater, L.J. (2014) Objective extraction of channel heads from high-resolution topographic data. *Water Resources Research*, 50(5), 4283–4304. Available from: <https://doi.org/10.1002/2013WR015167>
- Copons, R., Vilaplana, J.M. & Linares, R. (2009) Rockfall travel distance analysis by using empirical models (Solà d'Andorra La Vella, Central Pyrenees). *Natural Hazards and Earth System Sciences*, 9(6), 2107–2118. Available from: <https://doi.org/10.5194/nhess-9-2107-2009>
- Dahlquist, M.P. & West, A.J. (2019) Initiation and runout of post-seismic debris flows: Insights from the 2015 Gorkha earthquake. *Geophysical Research Letters*, 46(16), 9658–9668. Available from: <https://doi.org/10.1029/2019GL083548>
- Daido, A. (1971) On the occurrence of mud-debris flow. *Bulletin of the Disaster Prevention Research Institute*, 21(2), 109–135.
- DiBiase, R.A. & Ferrier, K.L. (2020) Southern California bedrock landscapes 2015 airborne Lidar. National Center for Airborne Laser Mapping (NCALM). Distributed by OpenTopography. Available from: <https://doi.org/10.5069/G9J38QPM>
- DiBiase, R.A., Heimsath, A.M. & Whipple, K.X. (2012) Hillslope response to tectonic forcing in threshold landscapes. *Earth Surface Processes and Landforms*, 37(8), 855–865. Available from: <https://doi.org/10.1002/esp.3205>
- DiBiase, R.A., Rossi, M.W. & Neely, A.B. (2018) Fracture density and grain size controls on the relief structure of bedrock landscapes. *Geology*, 46(5), 399–402. Available from: <https://doi.org/10.1130/G40006.1>
- DiBiase, R.A. & Whipple, K.X. (2011) The influence of erosion thresholds and runoff variability on the relationships among topography, climate, and erosion rate. *Journal of Geophysical Research*, 116(F4), F04036. Available from: <https://doi.org/10.1029/2011JF002095>
- DiBiase, R.A., Whipple, K.X., Heimsath, A.M. & Ouimet, W.B. (2010) Landscape form and millennial erosion rates in the San Gabriel Mountains, CA. *Earth and Planetary Science Letters*, 289(1–2), 134–144. Available from: <https://doi.org/10.1016/j.epsl.2009.10.036>
- Dietrich, W. (2014) Eel River critical zone observatory July 2014 Lidar survey. National Center for Airborne Laser Mapping (NCALM). Distributed by OpenTopography. Available from: <https://doi.org/10.5069/G9MP517V>
- DOGAMI. (2011) Oregon Department of Geology and Mineral Industries Lidar Program airborne lidar survey. Oregon Department of Geology and Mineral Industries (DOGAMI). Distributed by OpenTopography. Available from: <https://doi.org/10.5069/G9QC01D1>
- Ferguson, R. (2007) Flow resistance equations for gravel-and boulder-bed streams. *Water Resources Research*, 43(5), W05427. Available from: <https://doi.org/10.1029/2006WR005422>
- Finnegan, N.J., Klier, R.A., Johnstone, S., Pfeiffer, A.M. & Johnson, K. (2017) Field evidence for the control of grain size and sediment supply on steady-state bedrock river channel slopes in a tectonically active setting. *Earth Surface Processes and Landforms*, 42(14), 2338–2349. Available from: <https://doi.org/10.1002/esp.4187>
- Flint, J.J. (1974) Stream gradient as a function of order, magnitude, and discharge. *Water Resources Research*, 10(5), 969–973. Available from: <https://doi.org/10.1029/WR010i005p00969>
- Forte, A.M. & Whipple, K.X. (2018) Criteria and tools for determining drainage divide stability. *Earth and Planetary Science Letters*, 493, 102–117. Available from: <https://doi.org/10.1016/j.epsl.2018.04.026>
- Fratkin, M.M., Segura, C. & Bywater-Reyes, S. (2020) The influence of lithology on channel geometry and bed sediment Organization in Mountainous Hillslope-coupled Streams. *Earth Surface Processes and Landforms*, 45(10), 2365–2379. Available from: <https://doi.org/10.1002/esp.4885>
- Fuller, T.K., Perg, L.A., Willenbring, J.K. & Lepper, K. (2009) Field evidence for climate-driven changes in sediment supply leading to Strath terrace formation. *Geology*, 37(5), 467–470. Available from: <https://doi.org/10.1130/G25487A.1>
- Gartner, J.E., Cannon, S.H. & Santi, P.M. (2014) Empirical models for predicting volumes of sediment deposited by debris flows and sediment-laden floods in the transverse ranges of Southern California. *Engineering Geology*, 176, 45–56. Available from: <https://doi.org/10.1016/j.enggeo.2014.04.008>
- Hatchett, B.J., Cao, Q., Dawson, P.B., Ellis, C.J., Hecht, C.W., Kawzenuk, B., et al. (2020) Observations of an extreme atmospheric river storm with a diverse sensor network. *Earth and Space Science*, 7(8), e2020EA001129. Available from: <https://doi.org/10.1029/2020EA001129>
- Heimsath, A.M., DiBiase, R.A. & Whipple, K.X. (2012) Soil production limits and the transition to bedrock-dominated landscapes. *Nature Geoscience*, 5(3), 210–214. Available from: <https://doi.org/10.1038/ngeo1380>
- Hsu, L. (2015) *Field observations of bedrock channels scoured by debris flows*. Figshare Available from: <https://doi.org/10.6084/M9.FIGSHARE.1309500>
- Hungr, O., McDougall, S. & Bovis, M. (2005) Entrainment of material by debris flows. In: Jakob, M. & Hungr, O. (Eds.) *Debris-flow hazards and related phenomena*. Berlin, Heidelberg: Springer Praxis Books. Springer, pp. 135–158. Available from: [https://doi.org/10.1007/3-540-27129-5\\_7](https://doi.org/10.1007/3-540-27129-5_7)
- Hürlimann, M., Rickenmann, D. & Graf, C. (2003) Field and monitoring data of debris-flow events in the Swiss Alps. *Canadian Geotechnical Journal*, 40(1), 161–175. Available from: <https://doi.org/10.1139/t02-087>
- Jennings, C.W., Strand, R.G. & Rogers, T.H. (1977) *Geologic map of California*, 1:750,000. California Division of Mines and Geology Sacramento, CA.
- Johnson, J.P.L., Whipple, K.X., Sklar, L.S. & Hanks, T.C. (2009) Transport slopes, sediment cover, and Bedrock Channel incision in the Henry Mountains, Utah. *Journal of Geophysical Research, Earth Surface*, 114(F2), F02014. Available from: <https://doi.org/10.1029/2007JF000862>
- Kean, J.W., Staley, D.M. & Cannon, S.H. (2011) In situ measurements of post-fire debris flows in Southern California: Comparisons of the timing and magnitude of 24 debris-flow events with rainfall and soil moisture conditions. *Journal of Geophysical Research, Earth Surface*, 116(F4), F04019. Available from: <https://doi.org/10.1029/2011JF002005>
- Kean, J.W., Staley, D.M., Lancaster, J.T., Rengers, F.K., Swanson, B.J., Coe, J.A., et al. (2019) Inundation, flow dynamics, and damage in the 9 January 2018 Montecito debris-flow event, California, USA: Opportunities and challenges for post-wildfire risk assessment. *Geosphere*, 15(4), 1140–1163. Available from: <https://doi.org/10.1130/GES02048.1>
- Lague, D. (2014) The stream Power River incision model: Evidence, theory and beyond. *Earth Surface Processes and Landforms*, 39(1), 38–61. Available from: <https://doi.org/10.1002/esp.3462>
- Lague, D. & Davy, P. (2003) Constraints on the long-term colluvial erosion law by analyzing slope-area relationships at various tectonic uplift rates in the Siwaliks Hills (Nepal). *Journal of Geophysical Research, Solid Earth*, 108(B2), 2129. Available from: <https://doi.org/10.1029/2002JB001893>
- Lai, L.S.-H., Roering, J.J., Finnegan, N.J., Dorsey, R.J. & Yen, J.-Y. (2021) Coarse sediment supply sets the slope of bedrock channels in rapidly uplifting terrain: Field and topographic evidence from eastern Taiwan. *Earth Surface Processes and Landforms*, 46(13), 2671–2689. Available from: <https://doi.org/10.1002/esp.5200>
- Lamb, M.P., Dietrich, W.E. & Venditti, J.G. (2008) Is the critical shields stress for incipient sediment motion dependent on channel-bed slope? *Journal of Geophysical Research, Earth Surface*, 113(F2), F02008. Available from: <https://doi.org/10.1029/2007JF000831>
- Lamb, M.P., Scheingross, J.S., Amidon, W.H., Swanson, E. & Limaye, A. (2011) A model for fire-induced sediment yield by dry ravel in steep landscapes. *Journal of Geophysical Research, Earth Surface*, 116(F3), F03006. Available from: <https://doi.org/10.1029/2010JF001878>
- Lavé, J. & Burbank, D. (2004) Denudation processes and rates in the transverse ranges, southern California: Erosional response of a transitional

- landscape to external and anthropogenic forcing. *Journal of Geophysical Research, Earth Surface*, 109(F1), F01006. Available from: <https://doi.org/10.1029/2003JF000023>
- Li, G., West, A.J., Densmore, A.L., Hammond, D.E., Jin, Z., Zhang, F., et al. (2016) Connectivity of earthquake-triggered landslides with the fluvial network: Implications for landslide sediment transport after the 2008 Wenchuan earthquake. *Journal of Geophysical Research, Earth Surface*, 121(4), 703–724. Available from: <https://doi.org/10.1002/2015JF003718>
- Loucks, E. (2020) *The role of sediment grain size and bedrock abundance in setting the morphology of headwater channels in McKittrick canyon in the Guadalupe Mountains, NM/TX, USA.* BS Thesis. The Pennsylvania State University, State College, PA. Available from: [https://honors.libraries.psu.edu/files/final\\_submissions/6684](https://honors.libraries.psu.edu/files/final_submissions/6684)
- Mair, D., Do Prado, A.H., Garefalakis, P., Lechmann, A., Whittaker, A. & Schlunegger, F. (2022) Grain size of fluvial gravel bars from close-range UAV imagery – Uncertainty in segmentation-based data. *Earth Surface Dynamics*, 10(5), 953–973. Available from: <https://doi.org/10.5194/esurf-10-953-2022>
- Marc, O., Turowski, J.M. & Meunier, P. (2021) Controls on the grain size distribution of landslides in Taiwan: The influence of drop height, scar depth and bedrock strength. *Earth Surface Dynamics*, 9(4), 995–1011. Available from: <https://doi.org/10.5194/esurf-9-995-2021>
- McGuire, L.A., McCoy, S.W., Marc, O., Struble, W. & Barnhart, K.R. (2022) Steady-state forms of channel profiles shaped by debris-flow and fluvial processes. *Earth Surface Dynamics Discussions* (Preprint). Available from: <https://doi.org/10.5194/esurf-2022-47>
- Montgomery, D.R. & Dietrich, W.E. (1988) Where Do Channels Begin? *Nature*, 336(6196), 232–234. Available from: <https://doi.org/10.1038/336232a0>
- Montgomery, D.R. & Foufoula-Georgiou, E. (1993) Channel network source representation using digital elevation models. *Water Resources Research*, 29(12), 3925–3934. Available from: <https://doi.org/10.1029/93WR02463>
- Montgomery, D.R. & Gran, K.B. (2001) Downstream variations in the width of bedrock channels. *Water Resources Research*, 37(6), 1841–1846. Available from: <https://doi.org/10.1029/2000WR900393>
- Moon, S. (2012) *Northern California coast: Slope failure in low and high uplift regions.* Distributed by OpenTopography. Available from: <https://doi.org/10.5069/G9N29TWH>
- Moon, S., Merritts, D.J., Snyder, N.P., Bierman, P., Sanquini, A., Fosdick, J. C., et al. (2018) Erosion of coastal drainages in the Mendocino triple junction region (MTJ), northern California. *Earth and Planetary Science Letters*, 502, 156–165. Available from: <https://doi.org/10.1016/j.epsl.2018.09.006>
- Murphy, B.P., Johnson, J.P.L., Gasparini, N.M. & Sklar, L.S. (2016) Chemical weathering as a mechanism for the climatic control of Bedrock River incision. *Nature*, 532(7598), 223–227. Available from: <https://doi.org/10.1038/nature17449>
- National Weather Service. (2017) *A history of significant weather events in Southern California organized by weather type.* Available from: <https://www.weather.gov/media/sgx/documents/weatherhistory.pdf>
- Neely, A. (2019) *Quantifying rock strength controls in Guadalupe Mountains, NM/TX.* National Center for Airborne Laser Mapping (NCALM). Distributed by OpenTopography. Available from: <https://doi.org/10.5069/G9BK19G8>
- Neely, A., DiBiase, R.A. & Loucks, E.A. (2021) *McKittrick canyon Reef Trail strat section, Guadalupe Mtns Nat. Park, TX.* Distributed by OpenTopography. Available from: <https://doi.org/10.5069/G99C6VM6>
- Neely, A.B. & DiBiase, R.A. (2020) Drainage area, bedrock fracture spacing, and weathering controls on landscape-scale patterns in surface sediment grain size. *Journal of Geophysical Research, Earth Surface*, 125(10), e2020JF005560. Available from: <https://doi.org/10.1029/2020JF005560>
- Neely, A.B., DiBiase, R.A., Corbett, L.B., Bierman, P.R. & Caffee, M.W. (2019) Bedrock fracture density controls on hillslope erodibility in steep, rocky landscapes with patchy soil cover, Southern California, USA. *Earth and Planetary Science Letters*, 522, 186–197. Available from: <https://doi.org/10.1016/j.epsl.2019.06.011>
- Palucis, M.C. & Lamb, M.P. (2017) What Controls Channel form in Steep Mountain streams? *Geophysical Research Letters*, 44(14), 7245–7255. Available from: <https://doi.org/10.1002/2017GL074198>
- Parker, C., Clifford, N.J. & Thorne, C.R. (2011) Understanding the influence of slope on the threshold of coarse grain motion: Revisiting critical stream power. *Geomorphology*, 126(1–2), 51–65. Available from: <https://doi.org/10.1016/j.geomorph.2010.10.027>
- Penserini, B.D., Roering, J.J. & Streig, A. (2017) A morphologic proxy for debris flow erosion with application to the earthquake deformation cycle, Cascadia subduction zone, USA. *Geomorphology*, 282, 150–161. Available from: <https://doi.org/10.1016/j.geomorph.2017.01.018>
- Phillips, C.B. & Jerolmack, D.J. (2016) Self-Organization of River Channels as a critical filter on climate signals. *Science*, 352(6286), 694–697. Available from: <https://doi.org/10.1126/science.aad3348>
- Prancevic, J.P. & Lamb, M.P. (2015a) Particle friction angles in Steep Mountain channels. *Journal of Geophysical Research, Earth Surface*, 120(2), 242–259. Available from: <https://doi.org/10.1002/2014JF003286>
- Prancevic, J.P. & Lamb, M.P. (2015b) Unraveling bed slope from relative roughness in initial sediment motion. *Journal of Geophysical Research, Earth Surface*, 120(3), 474–489. Available from: <https://doi.org/10.1002/2014JF003323>
- Prancevic, J.P., Lamb, M.P. & Fuller, B.M. (2014) Incipient sediment motion across the river to debris-flow transition. *Geology*, 42(3), 191–194. Available from: <https://doi.org/10.1130/G34927.1>
- Reneau, S.L., Dietrich, W.E., Donahue, D.J., Jull, A.J.T. & Rubin, M. (1990) Late Quaternary history of Colluvial deposition and erosion in hollows, Central California coast ranges. *Geological Society of America Bulletin*, 102(7), 969–982. Available from: [https://doi.org/10.1130/0016-7606\(1990\)102<0969:LQHOCD>2.3.CO;2](https://doi.org/10.1130/0016-7606(1990)102<0969:LQHOCD>2.3.CO;2)
- Rengers, F.K., McGuire, L.A., Kean, J.W., Staley, D.M., Dobre, M., Robichaud, P.R., et al. (2021) Movement of sediment through a burned landscape: Sediment volume observations and model comparisons in the San Gabriel Mountains, California, USA. *Journal of Geophysical Research, Earth Surface*, 126(7), e2020JF006053. Available from: <https://doi.org/10.1029/2020JF006053>
- Roda-Boluda, D.C., D'Arcy, M., McDonald, J. & Whittaker, A.C. (2018) Lithological controls on hillslope sediment supply: Insights from landslide activity and grain size distributions. *Earth Surface Processes and Landforms*, 43(5), 956–977. Available from: <https://doi.org/10.1002/esp.4281>
- Rossi, M.W., Anderson, R.S., Anderson, S.P. & Tucker, G.E. (2020) Orographic controls on subdaily rainfall statistics and flood frequency in the Colorado front range, USA. *Geophysical Research Letters*, 47(4), e2019GL085086. Available from: <https://doi.org/10.1029/2019GL085086>
- Scheingross, J.S., Winchell, E.W., Lamb, M.P. & Dietrich, W.E. (2013) Influence of bed patchiness, slope, grain hiding, and form drag on gravel mobilization in very steep streams. *Journal of Geophysical Research, Earth Surface*, 118(2), 982–1001. Available from: <https://doi.org/10.1002/jgrf.20067>
- Schmidt, K.M., Roering, J.J., Stock, J.D., Dietrich, W.E., Montgomery, D.R. & Schaub, T. (2001) The variability of root cohesion as an influence on shallow landslide susceptibility in the Oregon coast range. *Canadian Geotechnical Journal*, 38(5), 995–1024. Available from: <https://doi.org/10.1139/t01-031>
- Schwanhart, W. & Scherler, D. (2014) Short communication: TopoToolbox 2 – MATLAB-based software for topographic analysis and modeling in earth surface sciences. *Earth Surface Dynamics*, 2(1), 1–7. Available from: <https://doi.org/10.5194/esurf-2-1-2014>
- Scott, K.M. (1971) *Origin and sedimentology of 1969 debris flows near Glendora, California.* U.S. Government Printing Office, Washington, DC. US Geological Survey Professional Paper, Vol. 750, pp. 242–247.
- Sklar, L.S. & Dietrich, W.E. (2004) A mechanistic model for river incision into bedrock by Saltating bed load. *Water Resources Research*, 40(6), W06301. Available from: <https://doi.org/10.1029/2003WR002496>
- Sklar, L.S. & Dietrich, W.E. (2006) The role of sediment in controlling steady-state Bedrock Channel slope: Implications of the saltation-

- abrasion incision model. *Geomorphology*, 82(1–2), 58–83. Available from: <https://doi.org/10.1016/j.geomorph.2005.08.019>
- Sklar, L.S., Riebe, C.S., Marshall, J.A., Genetti, J., Leclere, S., Lukens, C. L., et al. (2017) The problem of predicting the size distribution of sediment supplied by hillslopes to rivers. *Geomorphology*, 277, 31–49. Available from: <https://doi.org/10.1016/j.geomorph.2016.05.005>
- Snyder, N.P., Whipple, K.X., Tucker, G.E. & Merritts, D.J. (2003) Channel response to tectonic forcing: Field analysis of stream morphology and hydrology in the Mendocino triple junction region, northern California. *Geomorphology*, 53(1–2), 97–127. Available from: [https://doi.org/10.1016/S0169-555X\(02\)00349-5](https://doi.org/10.1016/S0169-555X(02)00349-5)
- Staley, D.M., Kean, J.W. & Rengers, F.K. (2020) The recurrence interval of post-fire debris-flow generating rainfall in the southwestern United States. *Geomorphology*, 370, 107392. Available from: <https://doi.org/10.1016/j.geomorph.2020.107392>
- Stock, J. & Dietrich, W.E. (2003) Valley incision by debris flows: Evidence of a topographic signature. *Water Resources Research*, 39(4), 1089. Available from: <https://doi.org/10.1029/2001WR001057>
- Stock, J.D. & Dietrich, W.E. (2006) Erosion of Steepland valleys by debris flows. *Geological Society of America Bulletin*, 118(9–10), 1125–1148. Available from: <https://doi.org/10.1130/B25902.1>
- Takahashi, T. (1978) Mechanical characteristics of debris flow. *Journal of the Hydraulics Division*, 104(8), 1153–1169. Available from: <https://doi.org/10.1061/JYCEAJ.0005046>
- Tang, H., McGuire, L.A., Rengers, F.K., Kean, J.W., Staley, D.M. & Smith, J. B. (2019) Evolution of debris-flow initiation mechanisms and sediment sources during a sequence of Postwildfire rainstorms. *Journal of Geophysical Research, Earth Surface*, 124(6), 1572–1595. Available from: <https://doi.org/10.1029/2018JF004837>
- Tranel, L.M. & Happel, A.A. (2020) Evaluating escarpment evolution and bedrock erosion rates in the Western Guadalupe Mountains. West Texas and New Mexico. *Geomorphology*, 368, 107335. Available from: <https://doi.org/10.1016/j.geomorph.2020.107335>
- US Geological Survey. (2020) USGS one meter CA SoCal wildfires B1 2018, *United States geological survey 3D elevation program 1 meter digital elevation model*. <http://nationalmap.gov/elevation.html>
- Wells, W.G. (1982) The storms of 1978 and 1980 and their effect on sediment movement in the eastern San Gabriel front. In: *Storms, floods, and debris flows in Southern California and Arizona 1978 and 1980*, pp. 229–242. National Academy Press, Washington, D.C.
- Whipple, K.X., DiBiase, R.A., Crosby, B. & Johnson, J.P.L. (2022) 6.40 - Bedrock Rivers. In: Shroder, J.F. (Ed.) *Treatise on geomorphology*, Second edition. Academic Press, pp. 865–903. Available from: <https://doi.org/10.1016/B978-0-12-818234-5.00101-2>
- Zimmermann, A., Church, M. & Hassan, M.A. (2010) Step-pool stability: Testing the jammed state hypothesis. *Journal of Geophysical Research, Earth Surface*, 115(F2), F02008. Available from: <https://doi.org/10.1029/2009JF001365>

## SUPPORTING INFORMATION

Additional supporting information can be found online in the Supporting Information section at the end of this article.

### How to cite this article: Neely, A.B. & DiBiase, R.A. (2023)

Sediment controls on the transition from debris flow to fluvial channels in steep mountain ranges. *Earth Surface Processes and Landforms*, 48(7), 1342–1361. Available from: <https://doi.org/10.1002/esp.5553>